ELSEVIER

Contents lists available at ScienceDirect

International Journal of Solids and Structures

journal homepage: www.elsevier.com/locate/ijsolstr





Experiments and modeling of the thermo-mechanically coupled behavior of VHB

Keven Alkhoury ^a, Nikola Bosnjak ^b, Yueping Wang ^c, Howon Lee ^d, Siva Nadimpalli ^e, Shawn A. Chester ^{a,*}

- ^a Mechanical Engineering, New Jersey Institute of Technology, Newark, NJ 07102, USA
- ^b Sibley School of Mechanical and Aerospace Engineering, Cornell University, Ithaca, NY 14853, USA
- ^c Department of Mechanical and Aerospace Engineering, Rutgers University, Piscataway, NJ 08854, USA
- d Department of Mechanical Engineering, Seoul National University, Gwanak-gu, Seoul 08826, South Korea
- ^e Department of Mechanical Engineering, Michigan State University, East Lansing, MI 48824, USA

ARTICLE INFO

Keywords: Thermomechanical Viscoelastic Nonlinear Large deformation Rubbers VHB 4910

ABSTRACT

Temperature is well known to have a significant effect on the overall mechanical performance of viscoelastomers. In this work, we investigate the thermo-mechanically coupled behavior of VHB 4910 using a combined experimental and modeling approach. We first characterize the material behavior by performing a set of large deformation uniaxial experiments at different temperatures. We then model the observed thermo-mechanical behavior and calibrate that model to the uniaxial experiments. Lastly, the model is implemented as a user material subroutine in a finite element package for validation purposes. A key finding of this work is that while increasing the temperature stiffens the elastic contribution, it concurrently reduces the viscoelastic contribution to the overall behavior of VHB.

1. Introduction

Viscoelastomers are a common class of materials found in everyday life. Typically, applications have a wide significance and range from consumer applications such as shock absorbers in helmets, computer drives and shoe insoles, to much more complicated applications such as artificial organs (Lakes, 2009), and are invaluable in the modern standard of living. And even on a large scale, viscoelastomers are used as dampers for structural applications (Shen and Soong, 1995; Chang et al., 1995). This class of rubber-like materials is characterized by a polymeric network that is capable of large viscoelastic deformations. That characteristic, large viscoelastic deformation, has made this class of materials a good candidate for active polymers, such as electronic artificial muscles and dielectric elastomer actuators (Mirfakhrai et al., 2007)

Many active polymers are classified as viscoelastic because of their well known complex time-dependent behavior. The theory of small deformation viscoelasticity was developed to characterize the viscoelastic behavior for polymeric materials subjected to strains $\lesssim 0.5\%$ (Bower, 2009). However, most applications involving rubber-like materials are expected to operate at larger strains. As a result, large deformations must be taken into account for a constitutive model of viscoelastomers. Consequently a lot of work exists in the literature for the

isothermal room temperature large-deformation viscoelastic behavior of rubber-like materials (cf. eg., Valanis, 1966; Arruda and Boyce, 1993; Bergström and Boyce, 1998; Reese and Govindjee, 1998; Linder et al., 2011; Mao et al., 2017).

Additionally much work has gone into the thermo-mechanical behavior of polymers, ranging from rubber-like to glassy (cf. eg., Qi et al., 2008; Nguyen et al., 2008; Anand et al., 2009; Ames et al., 2009; Srivastava et al., 2010a,b; Castro et al., 2010; Santapuri et al., 2013; Mehnert et al., 2018; Liao et al., 2020a; Jordan et al., 2020; Yang et al., 2021; Mehnert et al., 2021a,b, and references within). Recent research has also addressed the temperature-dependent behavior of viscoelastomers, however most prior work mainly focused on the smalldeformation behavior (Djoković et al., 2000; Liu et al., 2006; Drozdov and Christiansen, 2008). As per large deformation work, Lion (1997a,b) was one of the first to explore the field. As well, Reese and Govindjee (1997) formulated a large deformation thermo-viscoelasticity theory, where both theoretical and numerical aspects in the thermo-viscoelastic coupled behavior were presented. Later, they extended the model to include the transient network theory, where polymeric chains are expected to steadily break and reform (Reese, 2003). More recently, the literature has been complemented by extensive experimental and modeling efforts on various viscoelastomers such as Ecoflex, VHB, and

E-mail address: shawn.a.chester@njit.edu (S.A. Chester).

Corresponding author.

SIL30, at different temperatures and strain rates (Liao et al., 2020a,b; Hossain and Liao, 2020). While Mehnert et al. (2021a) are among the most recent and comprehensive to account for the effect of temperature on the time-independent contribution, the details are still not agreed upon and differ based on material. In this paper we focus on the commercially available material VHB 4910. VHB, an electro-active polymer, has been extensively studied over the past decade, for being a great candidate for a variety of applications ranging from lightweight dielectric elastomers (Plante and Dubowsky, 2006; Wissler and Mazza, 2007; O'Halloran et al., 2008; Brochu and Pei, 2010) to replacing conventional rivets in construction (3M, 2020). This material is chosen for its common importance in industrial applications, and since the existing literature shows that VHB exhibits a pronounced temperature-dependent viscoelastic behavior (Hossain et al., 2012; Guo et al., 2015; Liao et al., 2020a).

The goal of this paper is to experimentally characterize the large-deformation behavior of VHB in stretch rate and temperature range of industrial relevance, and then create a validated thermo-mechanically coupled continuum level constitutive model that may be used for predictive simulation. Toward that goal, we have conducted uniaxial tensile experiments at a handful of fixed temperatures and stretch rates. The experimental data is then used for the development of a continuum level constitutive model. The proposed model is implemented as a user material subroutine in Abaqus/Standard (2021) for model validation.

The temperature-dependent viscoelastic behavior of VHB was characterized by conducting different experiments: (i) dynamic mechanical analysis (DMA); (ii) creep at multiple loads and temperatures; (iii) uniaxial load–unload at multiple stretch rates and temperatures; and (iv) stress relaxation at the same fixed temperatures. For the constitutive modeling, we follow a similar approach to Bosnjak et al. (2020) and as a foundation employ the Arruda–Boyce model (Arruda and Boyce, 1993) to capture the time-independent behavior, and the micromechanical approach of Linder et al. (2011) to capture the time-dependent behavior.

The remainder of this paper is organized as follows, in Section 2 we report our experimental methods for characterizing the non-ambient temperature testing of the VHB, as well as the corresponding results. In Section 3 we overview the continuum framework. In Sections 4 and 5 we present a thermo-mechanically coupled constitutive model which is then calibrated in Section 6. In Section 7, we summarize and verify our model, and validate the model and implementation in Section 8. Section 9 provides concluding remarks for this work.

2. Experiments

In this section we report our experimental methods for characterizing the non-linear temperature-dependent viscoelastic behavior of VHB, together with the accompanying results.

2.1. Experimental plan

The overall behavior of VHB is complex, including large deformation viscoelasticity, accordingly we have designed an experimental program to try and assess each component individually as is often done in the literature (Hossain et al., 2012; Liao et al., 2020a). First, Dynamic Mechanical Analysis (DMA) was performed to obtain the temperature-dependent storage modulus, loss modulus, and $\tan \delta$, parameters typically found in the theory of linear viscoelasticity. We then investigate the time-independent behavior of VHB by performing a set of large deformation creep tests at a number of different loads and fixed temperatures, specifically 0 °C, 24 °C, 40 °C, 50 °C, and 60 °C. And lastly, we probe the time-dependent behavior of VHB by performing a set of load–unload tests at different stretch rates and stress relaxation at those same fixed temperatures.

A minimum of 3 samples were tested for the experiments reported here investigating the time-dependent behavior in order to ensure repeatability.

As a major assumption for analyzing the experimental results, the temperature is assumed to be constant across the entire sample for all time during an experiment. Further details discussing the validity of that assumption are provided in Appendix A. Additionally, VHB 4910 has a coefficient of thermal expansion of 180 $\frac{\mu m}{m^{\circ}C}$ (3M, 2020), and is expected to thermally expand when above room temperature, and contract below room temperature. For that reason, to ensure that each experiment starts in a stress free state, we take care to grip our tensile samples on both ends only after heating/cooling to the desired temperature in the environmental chamber. We discuss the details of each set of experiments in what follows.

2.2. Dynamic mechanical analysis

Dynamic mechanical analysis (DMA) provides the standard parameters from the theory of linear viscoelasticity, specifically the storage modulus (E'), the loss modulus (E''), and the $\tan \delta$. DMA characterization of a VHB specimen was conducted on a dynamic mechanical analyzer (DMA850, TA Instruments) using a tensile loading mode. A 30 mm long, 6 mm wide, and 1 mm thick VHB specimen was put on the tension clamp overnight to remove any viscous contribution associated with the installation of the specimen. Specimens were precooled at -50° C for 10 min to achieve thermal equilibrium. An oscillating strain of 0.15% was applied at a 1 Hz frequency with a preload of 0.005 N and force track of 150%. The storage modulus E', the loss modulus E'', and $\tan \delta$ were measured as a function of temperature while the temperature was increased from -50° C to 90 °C at a rate of 1 °C/min.

The result from DMA experiment is shown in Fig. 1. It is noted that the storage modulus of VHB changes by more than three orders of magnitude from ~1300 MPa at $-50\,^{\circ}\text{C}$ (glassy) to ~0.15 MPa at 90 °C (rubbery), with a peak in $\tan\delta$ occurring near 4 °C. The noise at the high-temperature region is attributed to the very low stiffness of VHB at relatively high temperatures.

2.3. Uniaxial experiment preliminaries

For a uniaxial experiment on rubber-like materials we extensively employ two kinematic quantities, the stretch

$$\lambda = \frac{l}{l_0} = \frac{u + l_0}{l_0} = 1 + \frac{u}{l_0} \,, \tag{1}$$

and the stretch rate

$$\dot{\lambda} = \frac{\dot{u}}{l_0} \,, \tag{2}$$

where l is the instantaneous gauge length, l_0 is initial gauge length, u is the displacement, and \dot{u} is the velocity. We have chosen to perform our experiments under displacement control, and at a constant stretch rate. Therefore, we use (2) to prescribe the load frame crosshead velocity for a tension test at a constant stretch rate.

As is standard, the nominal, or engineering stress, P, is the force divided by the initial cross-sectional area ${\cal A}_0$

$$P = \frac{F}{A_0} \,. \tag{3}$$

2.4. Sample preparation

Tensile dog bone samples are extracted from commercially purchased VHB 4910 tape using an ASTM D638-V cutting die. The grip sections are then covered by tape for easy handling since the material is transparent, and also sticky. The nominal gauge section dimensions of our samples are 9.49 mm long, 3.18 mm wide, and 1 mm thick. However, the exact dimensions of each sample are measured right before testing using ImageJ (Rasband, 1997-2018) due to expected minor dimensional variations. Since Digital Image Correlation (DIC) analysis requires contrast, we apply a number of black lines using a permanent marker to the gauge section of our sample as can be seen in Fig. 2.

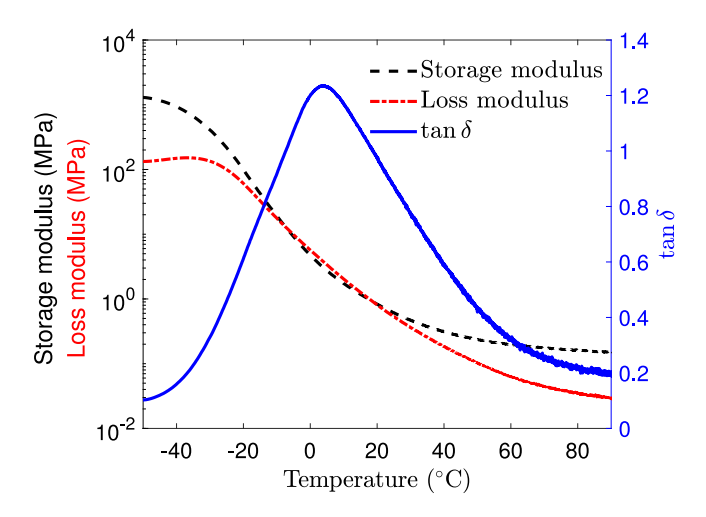


Fig. 1. DMA results for a temperature range of -50 °C to 90 °C.

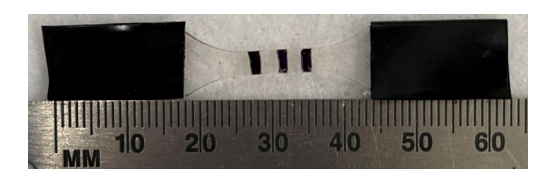


Fig. 2. Typical VHB specimen cut using an ASTM D638-V die. Note the black lines in the gauge section used for DIC and black tape on the grip sections used for easy handling.

2.5. Experimental setup

We performed tension tests using an MTS Criterion Model 43 uniaxial testing machine coupled with an environmental chamber (Thermcraft model LBO-24-10-10-11-5001). A picture of the load frame and chamber can be seen in Fig. 3. A loading rod is used to keep the sample visible through the environmental chamber window for the entire duration of an experiment so that we can capture its deformation using the camera. Further, to mitigate unwanted heat flow to the load cell, we use a temperature controlled fluid circulator (Polyscience SD07R-20-A11B) to maintain cooling water flowing transversely through the loading rod, having a cold water inlet and a hot water outlet, as seen in Fig. 3.

The relative humidity was measured and logged (Omega data logger model OM-73) and over the course of all experiments ranged from 13.3% to 33.4% with an average of 21.65%. The temperature inside the chamber is measured using three thermocouples placed at various locations. The temperature readings at all three locations were identical, therefore confirming an even temperature across the chamber.

A 2.5 pound load cell (Transducer Techniques MDB-2.5) is used to measure the force that is later used to calculate the stress. This load cell was chosen after several attempts to obtain the best signal-to-noise ratio in the measured data.

We use the DIC software Vic2D (Correlated Solutions) which is integrated with a digital camera (PointGrey GRAS-50S5M-C) to measure the stretch in our experiments. This is typical practice since measuring the deformation based on the crosshead displacement is known to be less accurate. Moreover, our DIC data acquisition system simultaneously captures images of the sample and force signal measurements, which is convenient when it comes to the post-processing since the deformation and force are synchronized in time.

Additionally, it is also known from the literature that so-called "heat waves" have been found to cause distortions in DIC measured strain fields at elevated temperatures (Jones and Reu, 2018; Ma et al., 2019).



Fig. 3. Experimental setup for uniaxial testing inside an environmental chamber at known temperatures. Here, 1 denotes the load cell, 2 the cold water inlet, 3 the hot water outlet, 4 the loading rod, 5 the (transparent) sample, and 6 the camera used for DIC.

Also, at cold temperatures, there is a possibility of condensation due to humidity in the air. For these reasons, we have performed some verification experiments, summarized in Appendix B, that indicate for the range of strains and temperatures used here, the DIC measurements are unaffected and reliable.

2.6. Uniaxial experiments

2.6.1. Creep

Creep experiments were performed by hanging various weights on the bottom of the dog bone tensile samples with the top held fixed, inside the environment chamber at a known temperature, and recording stretch data using DIC until the measured stretch reaches equilibrium. The samples measured here typically reached the equilibrium state within 12 h, when the stretch no longer changes over time, but for good measure the stretch data was recorded for a full 24 h. The use of different weights at a single temperature allows us to obtain the time-independent behavior for that temperature. Repeating at various temperatures allows us to obtain the temperature-dependent time-independent behavior.

2.6.2. Load-unload

To quantify rate-dependency we performed load–unload tensile tests to a maximum stretch of $\lambda=2$, at three different constant prescribed stretch rates $1\times 10^{-2}\,\mathrm{s}^{-1}$, $5\times 10^{-2}\,\mathrm{s}^{-1}$, and $1\times 10^{-1}\,\mathrm{s}^{-1}$. The prescribed loading profiles are shown in Fig. 4.

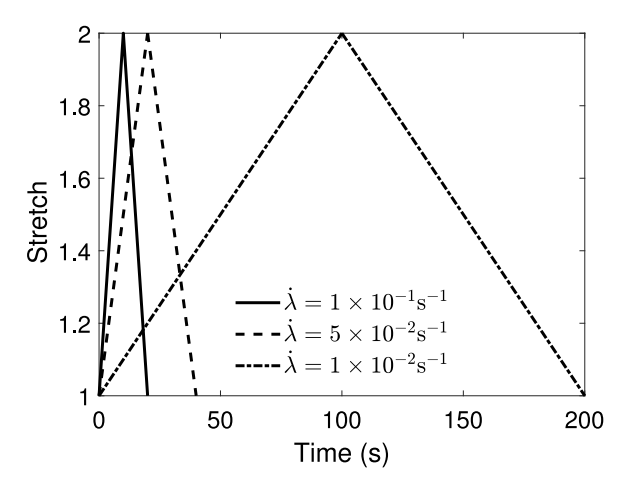


Fig. 4. Prescribed loading–unloading stretch profile to a maximum stretch of $\lambda = 2$.

Table 1 Measured initial stiffness, $\frac{dP}{dt}$, from creep results at various fixed temperatures.

Temperature (°C)	Initial stiffness (kPa)
0	51.19
24	54.60
40	58.50
50	58.50
60	58.50

2.6.3. Stress relaxation

A set of stress relaxation experiments were performed to probe the effect of temperature on the relaxation behavior of VHB. First, samples are loaded to a stretch $\lambda=3.5$, at a stretch rate of $\dot{\lambda}=2\times 10^{-1}\, \rm s^{-1}$, which is the fastest our screw driven testing machine can reliably move. Once the prescribed stretch is reached, the crosshead is held fixed for 1 h, while images for DIC and the force are recorded.

2.7. Uniaxial experimental results

The creep results are shown in Fig. 5. It can be observed from Fig. 5 that temperature affects the overall time-independent behavior of VHB 4910. Specifically, it can be observed that an increase in temperature affects both the initial stiffness and failure of VHB. That was further quantified by measuring the initial stiffness, $\frac{dP}{d\lambda}$ at $\lambda \approx 1$, and given in Table 1. From the data in Table 1, it is clear that an increase in temperature results in an increase in the initial stiffness up to 40 °C. The initial stiffness remains constant at all temperatures measured at 40 °C and above. Furthermore, clear chain-locking behavior is observed at room temperature at a uniaxial stretch of $\lambda \approx 9$, as the stiffness rapidly increases with a slight increase in stretch. However, the data indicates that as the temperature increases, the samples fail at a uniaxial stretch of $\lambda \approx 6$, much lower than room temperature samples. It can be concluded from the creep experiments that temperature plays a measurable role on the time-independent behavior of VHB.

The results of the load–unload tensile experiments are shown in Fig. 6. It can be clearly observed that VHB exhibits the expected behavior of a viscoelastomer, rate-dependence, hysteresis, and is clearly affected by the temperature. To quantify the effect of rate and temperature on the initial stiffness, we use the initial slope $\frac{dP}{d\lambda}$ evaluated at $\lambda \approx 1$ of the stress–stretch data and given in Table 2. From the data, for a fixed temperature, the initial stiffness rises as the stretch rate increases and is shown in Table 2 and Fig. 7a, and we observe a decrease in stiffness as the temperature increases. Overall, this shows that VHB becomes less viscous as the temperature increases.

Additionally, the hysteresis is quantified based on the area enclosed by the loading and unloading path on the stress-stretch curve and is

Table 2 Measured initial stiffness (kPa), $\frac{dP}{d\lambda}$ from load–unload tests at different prescribed stretch rates and temperatures.

Temperature (°C)	λ (s ⁻¹)		
	1×10^{-2}	5×10^{-2}	1×10^{-1}
0	502.48	941.56	1354.42
24	171.75	214.80	248.52
40	127.69	133.87	186.28
50	117.27	129.59	145.61
60	116.01	117.61	143.39

Table 3 Measured hysteresis (kPa) from load–unload tests for a stretch of $\lambda=2$ at different prescribed stretch rates and temperatures.

Temperature (°C)		$\dot{\lambda}$ (s ⁻¹))	
	1×10^{-2}	5×10^{-2}	1×10^{-1}	
0	83.44	161.62	224.99	
24	16.91	27.56	32.53	
40	13.83	15.65	19.62	
50	10.76	13.86	16.89	
60	12.24	11.56	14.77	

Table 4
Measured power law slope from the relaxation data at various fixed temperatures.

Temperature (°C)	Slope
0	-0.28
24	-0.11
40	-0.06
50	-0.05
60	-0.06

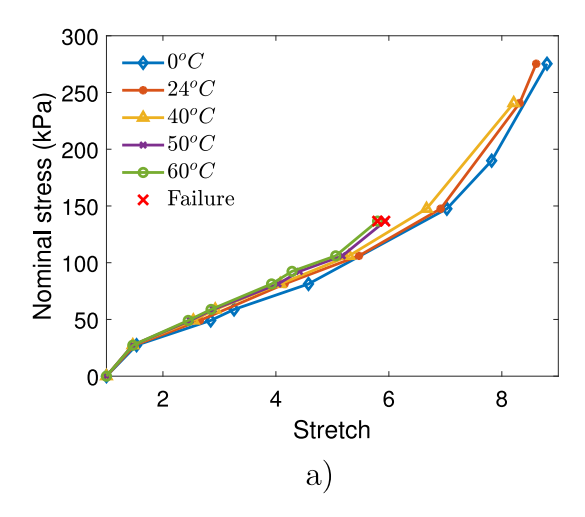
given in Table 3. One can observe that for a fixed temperature, the amount of hysteresis increases as the stretch rate increases and is shown in Table 3 and Fig. 7b. This trend holds for all cases except for a stretch rate $\dot{\lambda}=1\times 10^{-2}\,\mathrm{s^{-1}}$ at 60 °C, which may be due to the very low stiffness of the material at this temperature as seen in the DMA data in Fig. 1. Moreover, it can be noted that for a fixed stretch rate the amount of hysteresis decreases as the temperature increases. Likewise, this trend holds for all cases except for a stretch rate $\dot{\lambda}=1\times 10^{-2}\,\mathrm{s^{-1}}$ at 60 °C. Again, overall we find that VHB becomes less viscous as the temperature increases.

To sum up, the load–unload tensile experiments show a pronounced temperature-dependent viscoelastic behavior of VHB, where an increase in temperature reduces both the initial stiffness and the amount of the hysteresis, thereby an increase in temperature has the result of making VHB less viscoelastic. The overall summary is shown graphically in Fig. 7.

The results of the stress relaxation experiments are shown in Fig. 8. It is clearly observed that VHB exhibits stress relaxation. At room temperature (24 °C) the nominal stress relaxes from just over 168 kPa to roughly 78 kPa over the span of 1 h. The same trend holds for all the investigated temperatures. While the stress is expected to decrease over time during relaxation until it reaches an equilibrium state, the slope of the relaxation curve shown in Fig. 8f and tabulated in Table 4 is used as an indicator of the rate of relaxation. It can be observed that the relaxation slope tends towards equilibrium faster at higher temperatures. Also, one can notice that for temperatures higher than 40 °C, the influence of temperature on the relaxation behavior appears to saturate, leading to similar relaxation behavior for all our experiments above 40 °C.

3. Continuum framework

In this section we overview the kinematics and the governing continuum level equations to describe the thermo-mechanically coupled behavior of VHB.



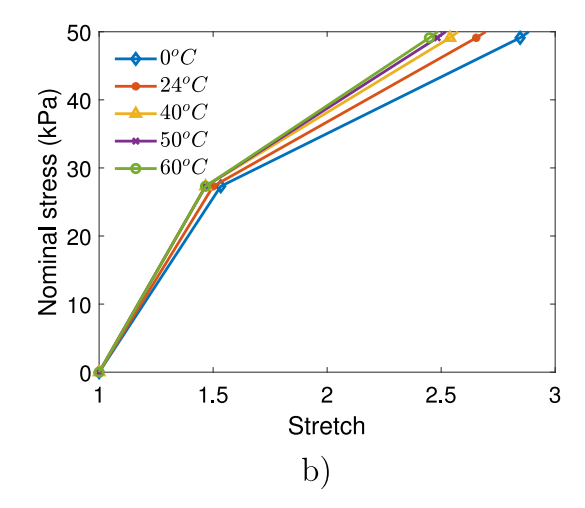


Fig. 5. (a) Large deformation creep results at different temperatures, and (b) close-up of the initial portion. Note that each curve is constructed from multiple individual creep tests run until equilibrium at a constant stress and temperature.

3.1. Kinematics

Consider an undeformed body \mathcal{B}_R identified with the region of space it occupies in a fixed reference configuration, and denote by \mathbf{x}_R an arbitrary material point of \mathcal{B}_R . The referential body \mathcal{B}_R then undergoes a motion $\mathbf{x} = \chi(\mathbf{x}_R, t)$ to the deformed body \mathcal{B}_t with deformation gradient given by

$$\mathbf{F} = \nabla \chi$$
, such that $J = \det \mathbf{F} > 0$. (4)

The right and left Cauchy-Green deformation tensors are given by

$$\mathbf{C} = \mathbf{F}^{\mathsf{T}} \mathbf{F},\tag{5}$$

and

$$\mathbf{B} = \mathbf{F} \mathbf{F}^{\mathsf{T}} \,. \tag{6}$$

Also, the polar decomposition of the deformation gradient

$$F = RU = VR \tag{7}$$

into a rotation \mathbf{R} , and the symmetric stretches \mathbf{U} and \mathbf{V} as is standard in the literature.

As is typical for viscoelastomers, we assume that the material is *nearly*-incompressible, and introduce the distortional and volumetric parts of the deformation gradient, defined as

$$\mathbf{F}_{\text{dis}} = J^{-1/3}\mathbf{F}$$
 where $\det \mathbf{F}_{\text{dis}} = 1$, (8)

and

$$\mathbf{F}_{\text{vol}} = J^{1/3} \mathbf{1}$$
 where $\det \mathbf{F}_{\text{vol}} = J$, (9)

so that

$$\mathbf{F} = \mathbf{F}_{\text{dis}} \mathbf{F}_{\text{vol}} \,. \tag{10}$$

The corresponding distortional right and left Cauchy–Green deformation tensors are then

$$\mathbf{C}_{\text{dis}} = \mathbf{F}_{\text{dis}}^{\mathsf{T}} \mathbf{F}_{\text{dis}} = J^{-2/3} \mathbf{C}, \tag{11}$$

and

$$\mathbf{B}_{\mathrm{dis}} = \mathbf{F}_{\mathrm{dis}} \mathbf{F}_{\mathrm{dis}}^{\mathsf{T}} = J^{-2/3} \mathbf{B} \,. \tag{12}$$

3.2. Balance laws

3.2.1. Balance of forces and moments

Neglecting inertial effects, the balance of forces and moments in the deformed body B_t are expressed as

$$\operatorname{div} \mathbf{T} + \mathbf{b} = \mathbf{0} \quad \text{and} \quad \mathbf{T} = \mathbf{T}^{\mathsf{T}}, \tag{13}$$

where T is the Cauchy stress and b the body force.

3.2.2. Balance of energy and the entropy imbalance

Following continuum mechanics convention and our previous work (Gurtin et al., 2010; Sain et al., 2018), we let ε and η represent the internal energy and entropy measured per unit mass in the deformed body, ρ the spatial mass density, \mathbf{q} denotes the heat flux measured per unit area in the deformed configuration, and q is the heat source/sink measured per unit volume in the deformed configuration. The first law of thermodynamics in the deformed body \mathcal{B}_{t} states that for an arbitrary part \mathcal{P}_{t} of the body with outward normal \mathbf{n}

$$\overline{\int_{\mathcal{P}_t} \rho \varepsilon dv} = -\int_{\partial \mathcal{P}_t} \mathbf{q} \cdot \mathbf{n} da + \int_{\mathcal{P}_t} q dv + \int_{\partial \mathcal{P}_t} \mathbf{T} \mathbf{n} \cdot \mathbf{v} da + \int_{\mathcal{P}_t} \mathbf{b} \cdot \mathbf{v} dv. \tag{14}$$

Since the part \mathcal{P}_r is arbitrary, we use the divergence theorem to obtain a local form of (14)

$$\rho \dot{\varepsilon} = -\text{div}\,\mathbf{q} + q + \mathbf{T} : \mathbf{L} \tag{15}$$

with velocity gradient $\mathbf{L} = \dot{\mathbf{F}}\mathbf{F}^{-1}.$ The stress power, T:L, admits the conventional decomposition

$$T: \mathbf{L} = \mathbf{T}: (\dot{\mathbf{F}}\mathbf{F}^{-1})$$

$$= J^{-1}\mathbf{T}_{\mathbf{R}}: \dot{\mathbf{F}}$$

$$= \frac{1}{2}J^{-1}\mathbf{S}: \dot{\mathbf{C}}$$
(16)

where we have introduced the stress measures

$$\mathbf{T}_{\mathbf{R}} = J\mathbf{T}\mathbf{F}^{-\mathsf{T}} \quad \text{and} \quad \mathbf{S} = J\mathbf{F}^{-1}\mathbf{T}\mathbf{F}^{-\mathsf{T}}$$
 (17)

as the first and second Piola stress, respectively. Accordingly, with use of (16) one can express the balance of energy in the following form

$$\rho \dot{\varepsilon} = -\operatorname{div} \mathbf{q} + q + \frac{1}{2} J^{-1} \mathbf{S} : \dot{\mathbf{C}}. \tag{18}$$

Additionally, for an arbitrary part P_t of the deformed body B_t , the second law takes the form of an entropy imbalance

$$\overline{\int_{\mathcal{P}_{t}} \rho \eta dv} \ge -\int_{\partial \mathcal{P}_{t}} \frac{\mathbf{q} \cdot \mathbf{n}}{\theta} da + \int_{\mathcal{P}_{t}} \frac{q}{\theta} dv, \tag{19}$$

where ϑ is the absolute temperature. Since the part \mathcal{P}_t is arbitrary, we can obtain the local form of (19) by using the divergence theorem

$$\rho \dot{\eta} \ge -\frac{1}{\theta} \operatorname{div} \mathbf{q} + \frac{1}{\theta^2} \mathbf{q} \cdot \operatorname{grad} \theta + \frac{q}{\theta} \,. \tag{20}$$

Next, let

$$\psi \stackrel{\text{def}}{=} \varepsilon - \vartheta \eta \tag{21}$$

express the Helmholtz free energy measured per unit deformed mass. Then (18) and (20), with (21), give in the local dissipation inequality

$$\rho \dot{\psi} + \rho \eta \dot{\theta} + \frac{1}{\vartheta} \mathbf{q} \cdot \operatorname{grad} \vartheta - \frac{1}{2} J^{-1} \mathbf{S} : \dot{\mathbf{C}} \le 0.$$
 (22)

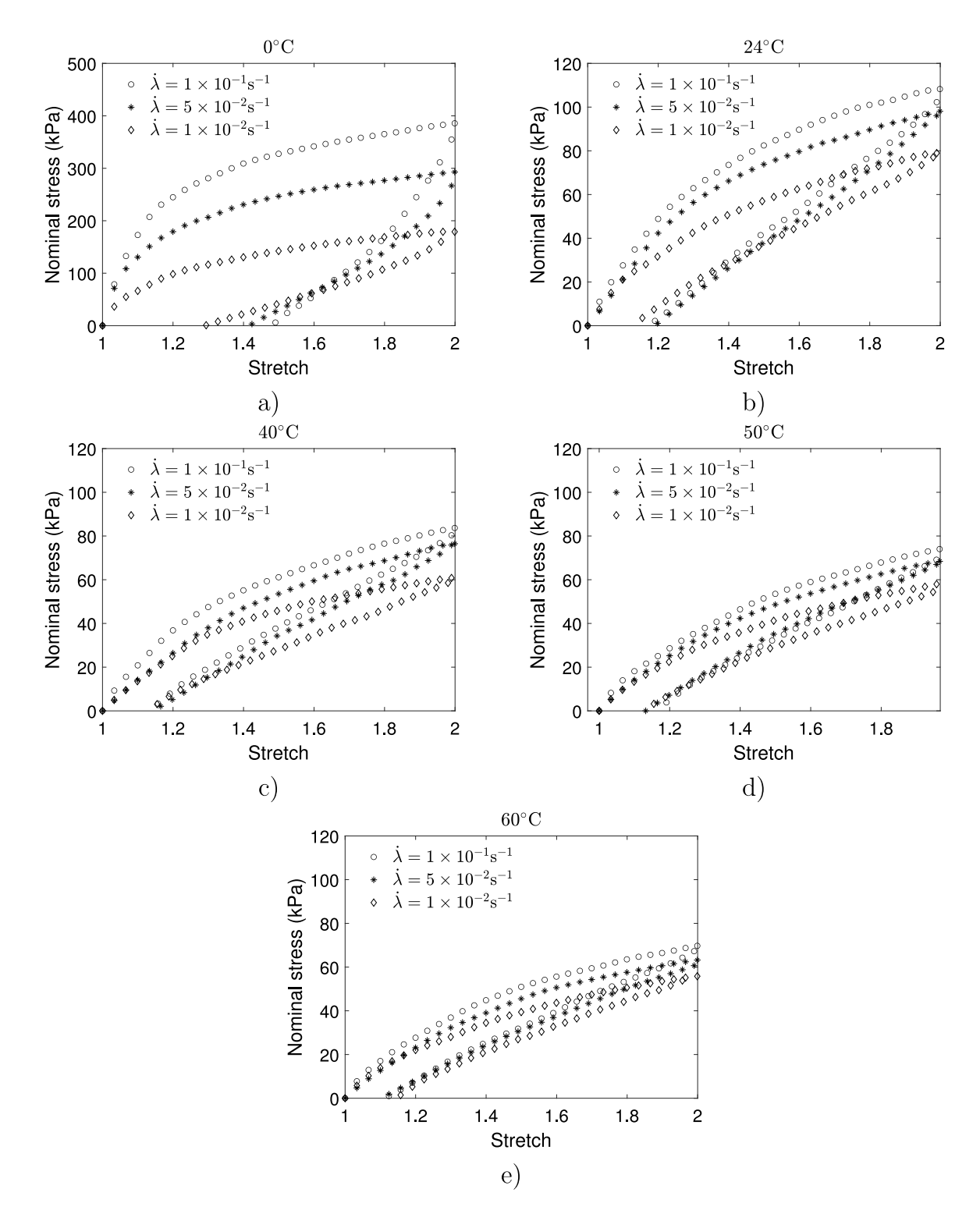


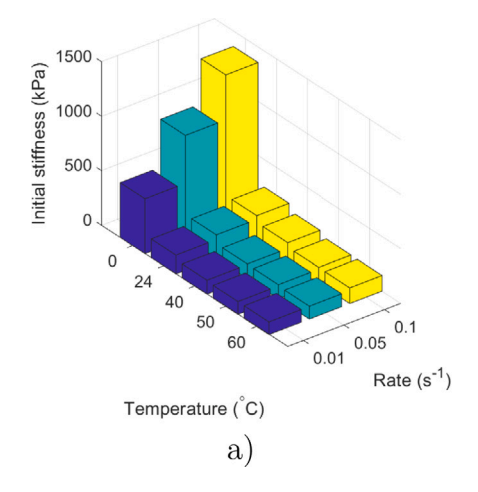
Fig. 6. Uniaxial experimental results for load–unload tests for different stretch rates and temperatures (a) 0 °C, (b) 24 °C, (c) 40 °C, (d) 50 °C, and (e) 60 °C. Note the change in scale for the data at 0 °C.

The referential quantities ψ_R , ε_R , η_R , \mathbf{q}_R , and $\nabla \vartheta$ are related to their spatial counterparts through the following relations

$$\begin{split} &\psi_{\mathrm{R}} = \rho J \psi, \quad \varepsilon_{\mathrm{R}} = \rho J \varepsilon, \quad \eta_{\mathrm{R}} = \rho J \eta \,, \quad \mathbf{q}_{\mathrm{R}} = J \mathbf{F}^{-1} \mathbf{q} \,, \\ &\text{and} \quad \nabla \theta = \mathbf{F}^{\mathsf{T}} \mathrm{grad} \, \theta \,, \end{split} \tag{23}$$

which can be used to rewrite the local dissipation inequality in the referential form

$$\dot{\psi}_{R} + \eta_{R}\dot{\vartheta} + \frac{1}{\vartheta}\mathbf{q}_{R} \cdot \nabla\vartheta - \frac{1}{2}\mathbf{S} : \dot{\mathbf{C}} \le 0.$$
 (24)



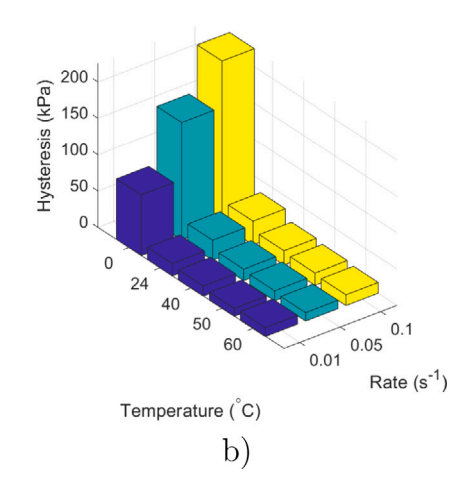


Fig. 7. (a) Initial stiffness (kPa), and (b) hysteresis (kPa) for different temperatures and stretch rates for load-unload tensile experiments.

It is worth mentioning that all terms in the dissipation inequality (24) are invariant under a frame transformation, since a change in frame does not affect referential fields.

4. Constitutive theory

4.1. Basic constitutive equations

As shown in the experimental observations provided in Section 2, we assume that the thermo-mechanically coupled mechanical response of VHB is viscoelastic and temperature-dependent. Since deformation history is important for viscoelastomers, we take an internal variable approach using γ tensorial internal variables denoted by $A^{(\gamma)}$. Based on the local dissipation inequality (24), we assume the following set of frame-indifferent basic constitutive equations

$$\psi_{\mathbf{R}} = \hat{\psi}_{\mathbf{R}}(\mathbf{C}, \mathbf{A}^{(\gamma)}, \vartheta)
\eta_{\mathbf{R}} = \hat{\eta}_{\mathbf{R}}(\mathbf{C}, \mathbf{A}^{(\gamma)}, \vartheta)
\mathbf{S} = \hat{\mathbf{S}}(\mathbf{C}, \mathbf{A}^{(\gamma)}, \vartheta)$$
(25)

along with evolution equations for the tensorial internal variables used to model the viscous behavior

$$\dot{\mathbf{A}}^{(\gamma)} = \dot{\mathbf{A}}^{(\gamma)}(\mathbf{C}, \mathbf{A}^{(\gamma)}, \vartheta), \quad \mathbf{A}^{(\gamma)}(\mathbf{x}_{\mathbf{R}}, t = 0) = 1. \tag{26}$$

Also, as is standard we express the heat flux following Fourier's law

$$\mathbf{q} = -\kappa(\theta) \operatorname{grad} \theta, \tag{27}$$

where κ is the scalar temperature-dependent thermal conductivity.

4.2. Thermodynamic restrictions

Starting with (25), we have

$$\dot{\psi}_{\rm R}({\bf C},{\bf A}^{(\gamma)},\vartheta) = \frac{\partial\psi_{\rm R}}{\partial{\bf C}}:\dot{\bf C} + \sum_{\gamma} \frac{\partial\psi_{\rm R}}{\partial{\bf A}^{(\gamma)}}:\dot{\bf A}^{(\gamma)} + \frac{\partial\psi_{\rm R}}{\partial\vartheta}\dot{\vartheta}, \tag{28}$$

then we make use of (27) and (28) in (24) to obtain

$$\left(\frac{\partial \psi_{R}}{\partial \mathbf{C}} - \frac{1}{2}\mathbf{S}\right) : \dot{\mathbf{C}} + \sum_{\gamma} \frac{\partial \psi_{R}}{\partial \mathbf{A}^{(\gamma)}} : \dot{\mathbf{A}}^{(\gamma)} + \left(\frac{\partial \psi_{R}}{\partial \vartheta} + \eta_{R}\right)
\times \dot{\vartheta} - \frac{J}{\vartheta} (\kappa \operatorname{grad} \vartheta) \cdot \operatorname{grad} \vartheta \le 0.$$
(29)

Further, (29) must always hold regardless of the choice of the constitutive equations and motions of the body, and therefore provides the state relations,

$$\mathbf{S} = 2 \frac{\partial \psi_{\mathbf{R}}(\mathbf{C}, \mathbf{A}^{(\gamma)}, \vartheta)}{\partial \mathbf{C}}$$

$$\eta_{\mathbf{R}} = -\frac{\partial \psi_{\mathbf{R}}(\mathbf{C}, \mathbf{A}^{(\gamma)}, \vartheta)}{\partial \vartheta}$$
(30)

and the reduced dissipation inequality

$$-\sum_{\gamma} \frac{\partial \psi_{\mathbf{R}}}{\partial \mathbf{A}^{(\gamma)}} : \dot{\mathbf{A}}^{(\gamma)} + \frac{J}{\vartheta}(\kappa \operatorname{grad} \vartheta) \cdot \operatorname{grad} \vartheta \ge 0.$$
 (31)

We additionally assume that the response is strictly dissipative so that

$$(\kappa \operatorname{grad} \theta) \cdot \operatorname{grad} \theta > 0 \quad \text{when} \quad \operatorname{grad} \theta \neq \mathbf{0},$$
 (32)

and

$$-\sum_{\gamma} \frac{\partial \psi_{R}}{\partial \mathbf{A}^{(\gamma)}} : \dot{\mathbf{A}}^{(\gamma)} > 0 \quad \text{when} \quad \dot{\mathbf{A}}^{(\gamma)} \neq \mathbf{0}.$$
 (33)

4.3. Further consequences of thermodynamics

Using (30) in (28) yields the first Gibbs relation

$$\dot{\psi}_{R} = \frac{1}{2}\mathbf{S} : \dot{\mathbf{C}} + \sum_{\gamma} \frac{\partial \psi_{R}}{\partial \mathbf{A}^{(\gamma)}} : \dot{\mathbf{A}}^{(\gamma)} - \eta_{R} \dot{\vartheta}. \tag{34}$$

Likewise, using $\psi_R = \varepsilon_R - \theta \eta_R$, one obtains the second Gibbs relation,

$$\dot{\varepsilon}_{R} = \frac{1}{2}\mathbf{S} : \dot{\mathbf{C}} + \sum_{\gamma} \frac{\partial \psi_{R}}{\partial \mathbf{A}^{(\gamma)}} : \dot{\mathbf{A}}^{(\gamma)} + \vartheta \dot{\eta}_{R} . \tag{35}$$

Next, we define the specific heat measured in energy per unit mass per temperature for a fixed deformation

$$C \stackrel{\text{def}}{=} \frac{\partial \varepsilon}{\partial \theta} = \frac{1}{\rho J} \frac{\partial \varepsilon_{R}}{\partial \theta} \,. \tag{36}$$

Using (30) we have

$$C = \frac{1}{\rho J} \left(\frac{\partial \psi_{R}}{\partial \theta} + \eta_{R} + \theta \frac{\partial \eta_{R}}{\partial \theta} \right) = -\frac{\theta}{\rho J} \frac{\partial^{2} \psi_{R}}{\partial \theta^{2}}.$$
 (37)

Next differentiating (30) results in

$$\dot{\eta}_{R} = -\frac{1}{2} \frac{\partial \mathbf{S}}{\partial \theta} : \dot{\mathbf{C}} - \frac{\partial^{2} \psi_{R}}{\partial \theta^{2}} \dot{\theta} - \frac{\partial}{\partial \theta} \left(\sum_{\gamma} \frac{\partial \psi_{R}}{\partial \mathbf{A}^{(\gamma)}} : \dot{\mathbf{A}}^{(\gamma)} \right), \tag{38}$$

which yields

$$\vartheta \dot{\eta_{\rm R}} = -\frac{1}{2}\vartheta \frac{\partial \mathbf{S}}{\partial \vartheta} : \dot{\mathbf{C}} + \rho J C \dot{\vartheta} - \vartheta \frac{\partial}{\partial \vartheta} \left(\sum_{\gamma} \frac{\partial \psi_{\rm R}}{\partial \mathbf{A}^{(\gamma)}} : \dot{\mathbf{A}}^{(\gamma)} \right). \tag{39}$$

Further, using (39) and (35) in (18) produces the heat equation in the deformed configuration

$$\rho C \dot{\theta} = \text{div}(\kappa \text{grad } \theta) + a$$

$$-J^{-1} \sum_{\gamma} \frac{\partial \psi_{R}}{\partial \mathbf{A}^{(\gamma)}} : \dot{\mathbf{A}}^{(\gamma)} + \frac{1}{2} J^{-1} \vartheta \frac{\partial \mathbf{S}}{\partial \vartheta} : \dot{\mathbf{C}} + J^{-1} \vartheta \frac{\partial}{\partial \vartheta}$$

$$\times \left(\sum_{\gamma} \frac{\partial \psi_{R}}{\partial \mathbf{A}^{(\gamma)}} : \dot{\mathbf{A}}^{(\gamma)} \right).$$
(40)

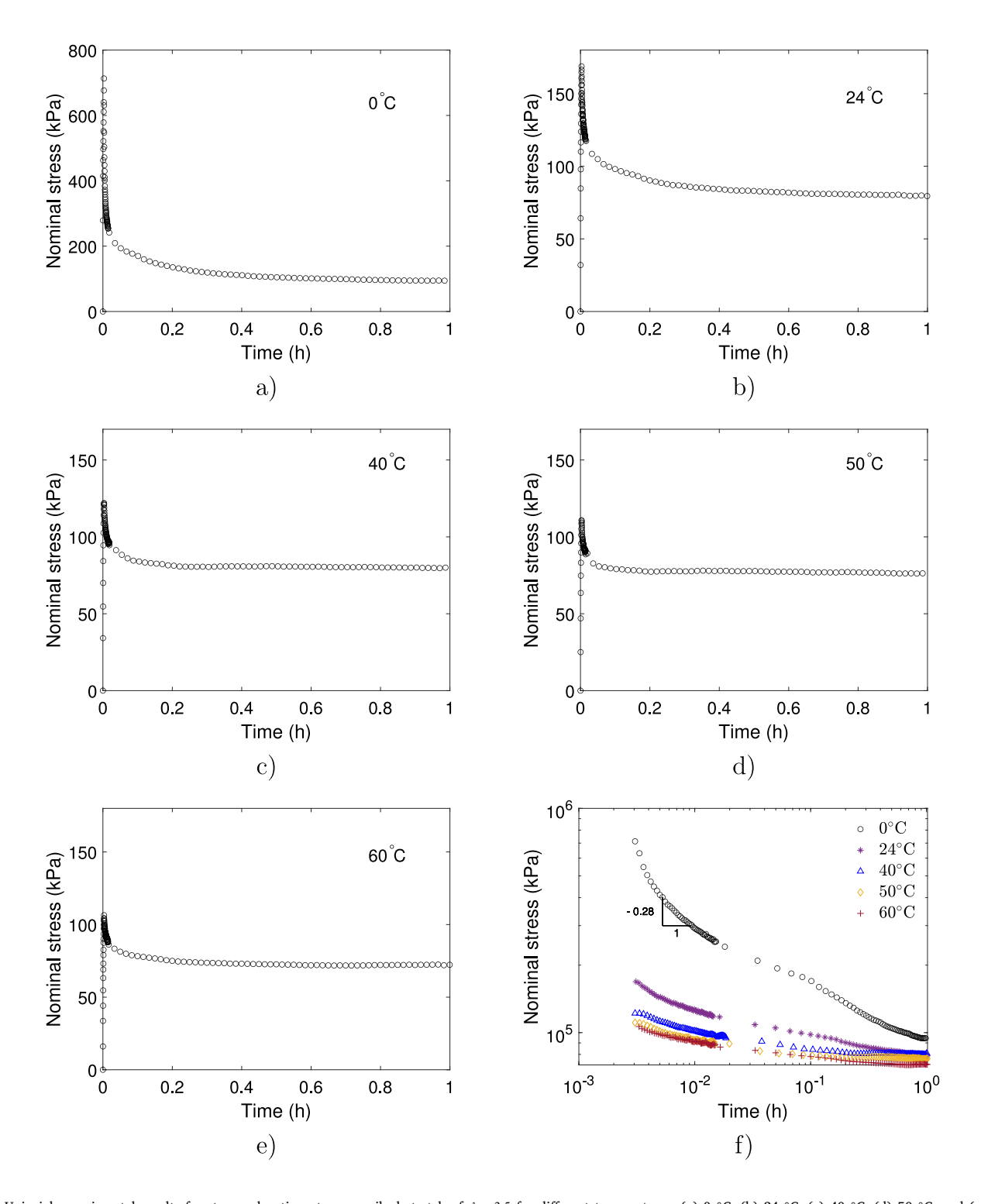


Fig. 8. Uniaxial experimental results for stress relaxation at a prescribed stretch of $\lambda = 3.5$ for different temperatures: (a) 0 °C, (b) 24 °C, (c) 40 °C, (d) 50 °C, and (e) 60 °C. (f) All relaxation data together on a log-log scale. Note the change in scale for the data at 0 °C. Also, we note that the spacing of data in time is due to a change in the data acquisition frequency during an experiment.

5. Specialized constitutive equations

In order to model the behavior of VHB 4910, we employ an additive decomposition of the free energy into time-independent (or elastic) and time-dependent (or viscous) parts as it is a common approach used in literature (Bergström and Boyce, 1998; Reese and Govind-

jee, 1998; Anand et al., 2009; Wang et al., 2016; Bosnjak et al., 2020). Specifically, we model the time-independent behavior by employing a non-Gaussian statistical mechanics model, which accounts for limiting chain extensibility (Arruda and Boyce, 1993), and for the time-dependent behavior we apply the micromechanically inspired model from Linder et al. (2011).

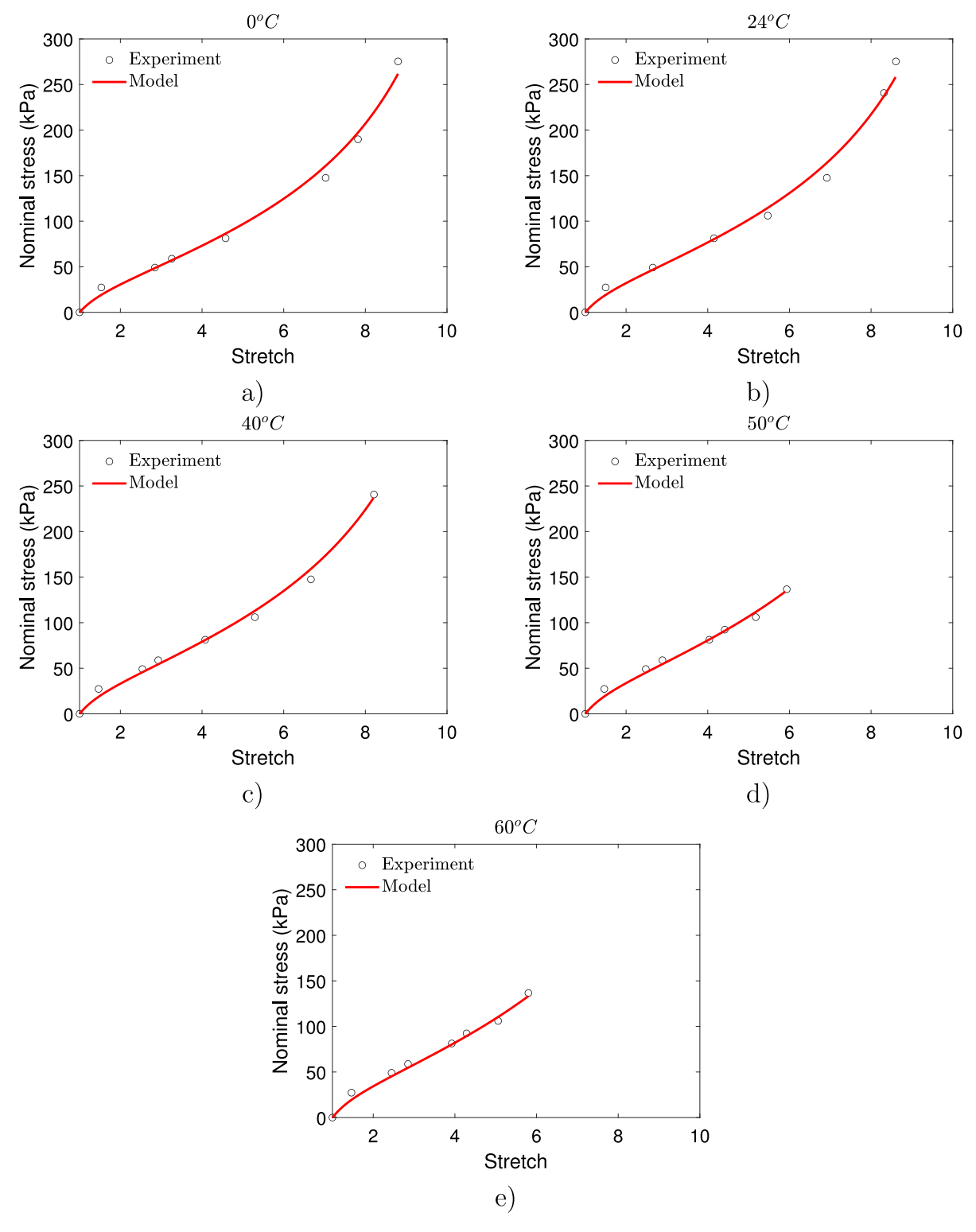


Fig. 9. Calibration of the time-independent behavior of VHB 4910 at different temperatures, (a) 0 °C, (b) 24 °C, (c) 40 °C, (d) 50 °C, and (e) 60 °C.

5.1. Free energy

We take the free energy function additively decomposed into two contributions

$$\hat{\psi}_{R}(\mathbf{C}_{dis}, J, \mathbf{A}^{(\gamma)}, \vartheta) = \hat{\psi}_{R}^{TI}(\mathbf{C}_{dis}, J, \vartheta) + \sum_{\gamma} \hat{\psi}_{R}^{TD(\gamma)}(\mathbf{C}_{dis}, J, \mathbf{A}^{(\gamma)}, \vartheta), \qquad (41)$$

where $\hat{\psi}_{\mathrm{R}}^{\mathrm{TI}}(\mathbf{C}_{\mathrm{dis}},J,\theta)$ is the time-independent contribution, and $\sum_{\gamma}\hat{\psi}_{\mathrm{R}}^{\mathrm{TD}(\gamma)}(\mathbf{C}_{\mathrm{dis}},J,\mathbf{A}^{(\gamma)},\theta)$ is the overall time-dependent contribution employing γ viscous mechanisms.

For the time-independent free energy we adopt the statistical mechanics based Arruda–Boyce model (Arruda and Boyce, 1993) which accounts for the chain locking behavior of the polymeric network. To incorporate temperature effects this contribution to the free energy is

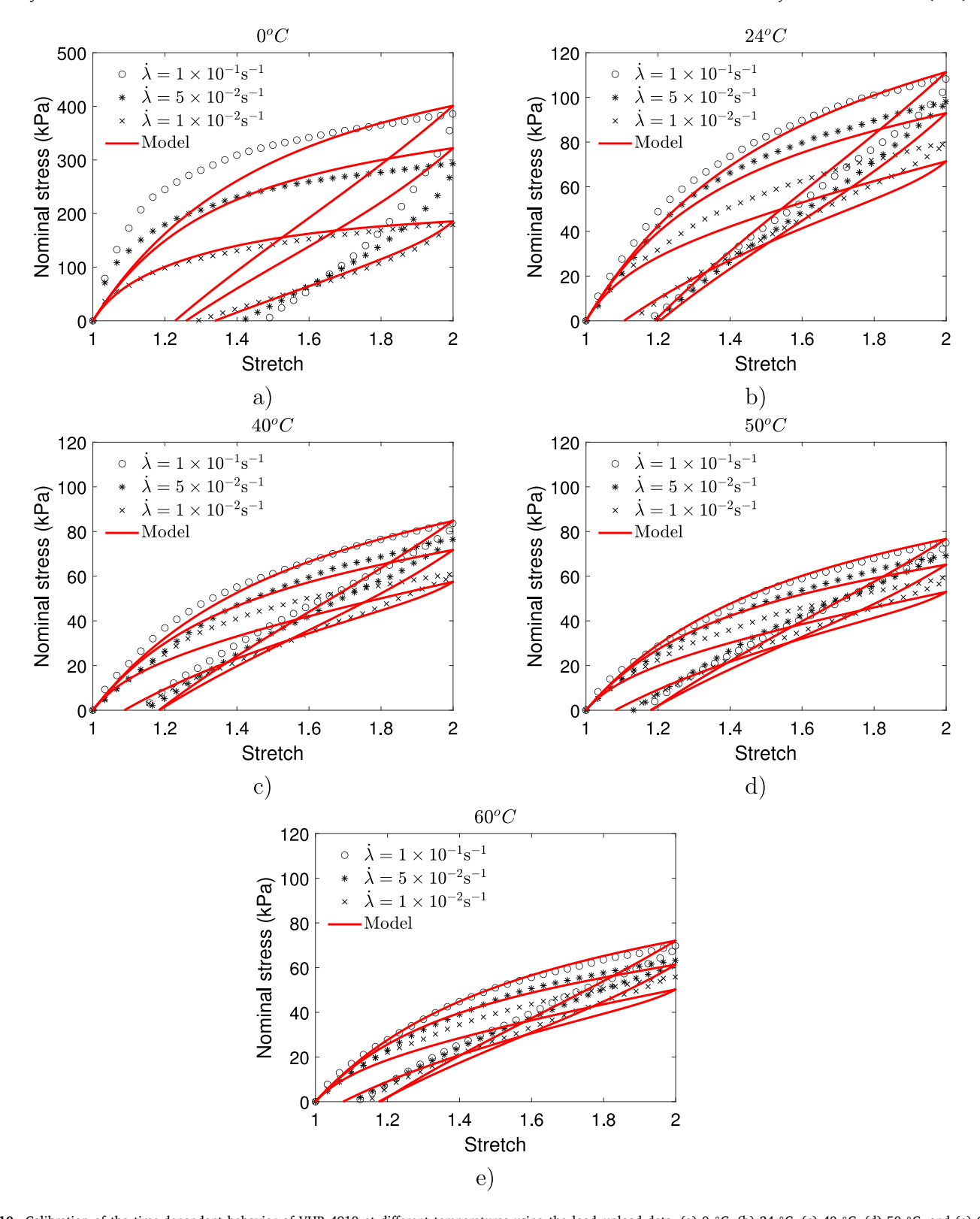


Fig. 10. Calibration of the time-dependent behavior of VHB 4910 at different temperatures using the load–unload data, (a) 0 °C, (b) 24 °C, (c) 40 °C, (d) 50 °C, and (e) 60 °C. Note the change in scale for the data at 0 °C.

assumed to have the following form

$$\begin{split} \hat{\psi}_{\mathrm{R}}^{\mathrm{TI}} &= \hat{G}_{0}\left(\vartheta\right) \lambda_{L}^{2} \left[\left(\frac{\bar{\lambda}}{\lambda_{L}} \right) \beta + \ln \left(\frac{\beta}{\sinh \beta} \right) - \left(\frac{1}{\lambda_{L}} \right) \beta_{0} - \ln \left(\frac{\beta_{0}}{\sinh \beta_{0}} \right) \right] \\ &+ \frac{1}{2} \hat{K}(\vartheta) (\ln J)^{2} - 3 \hat{K}(\vartheta) \alpha (\vartheta - \vartheta_{0}) (\ln J) \,, \end{split} \tag{42}$$

where $\hat{G}_0(\vartheta)$ is the temperature-dependent initial shear modulus, λ_L the constant locking stretch, and $\bar{\lambda}=\sqrt{\mathrm{tr}\,\mathbf{C}_{\mathrm{dis}}/3}$ the effective stretch. The functions β and β_0 are given by

$$\beta = \mathcal{L}^{-1} \left(\frac{\bar{\lambda}}{\lambda_L} \right) \quad \text{and} \quad \beta_0 = \mathcal{L}^{-1} \left(\frac{1}{\lambda_L} \right),$$
 (43)

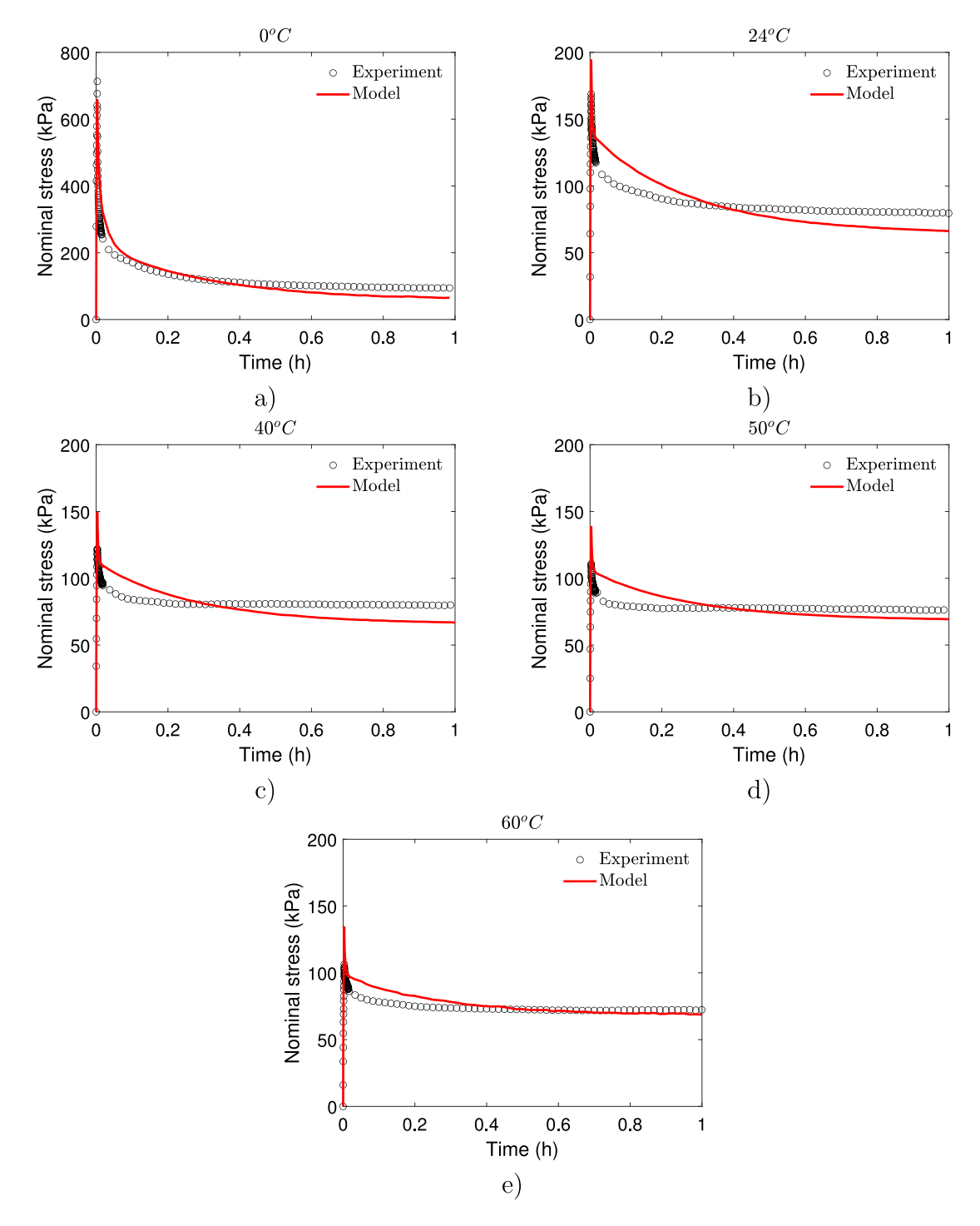


Fig. 11. Calibration of the time-dependent behavior of VHB 4910 at different temperatures using the relaxation data, (a) 0 °C, (b) 24 °C, (c) 40 °C, (d) 50 °C, and (e) 60 °C. Note the change in scale for the data at 0 °C.

where \mathcal{L}^{-1} is the inverse of the Langevin function, $\mathcal{L}(\bullet) = \coth(\bullet) - 1/(\bullet)$. Further, based on the experimental results, we take the temperature dependent modulus in the linear form

$$\hat{G}_0(\theta) = G_m \theta + G_b \,, \tag{44}$$

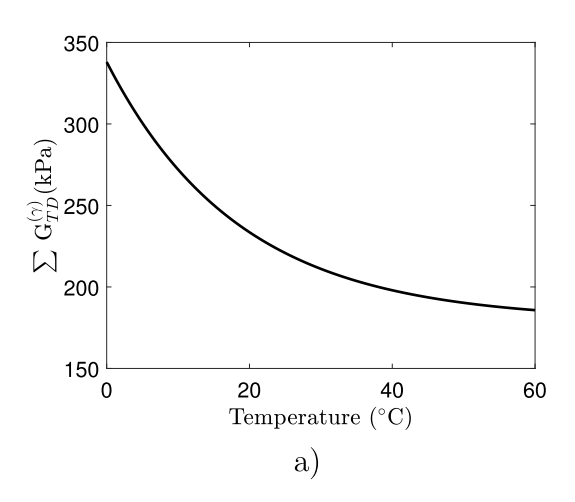
Additionally, $\hat{K}(\vartheta)$ is the bulk modulus used to approximate the near-incompressible conditions and is assumed to be three orders of magnitude greater than the shear modulus $\hat{G}_0(\vartheta)$, α is the coefficient of thermal expansion, and lastly ϑ_0 is a reference temperature.

For the time-dependent free energy, we follow the work of Linder et al. (2011), which for each viscous mechanism γ takes the form

$$\hat{\psi}_{R}^{TD(\gamma)} = \frac{1}{2} \hat{G}_{TD}^{(\gamma)}(\vartheta) \left[\left(\mathbf{A}^{(\gamma)} : \mathbf{C}_{dis} - 3 \right) - \ln \left(\det \mathbf{A}^{(\gamma)} \right) \right] , \tag{45}$$

where $\hat{G}_{TD}^{(\gamma)}(\vartheta)$ are the temperature-dependent shear moduli for each viscous mechanism γ , and based on the data are taken in the form

$$G_{\text{TD}}^{(\gamma)}(\vartheta) = G_{\text{TD}}^{c}{}^{(\gamma)} + G_{\text{TD}}^{d}{}^{(\gamma)} \exp\left(-G_{\text{TD}}^{e}{}^{(\gamma)}\vartheta\right). \tag{46}$$



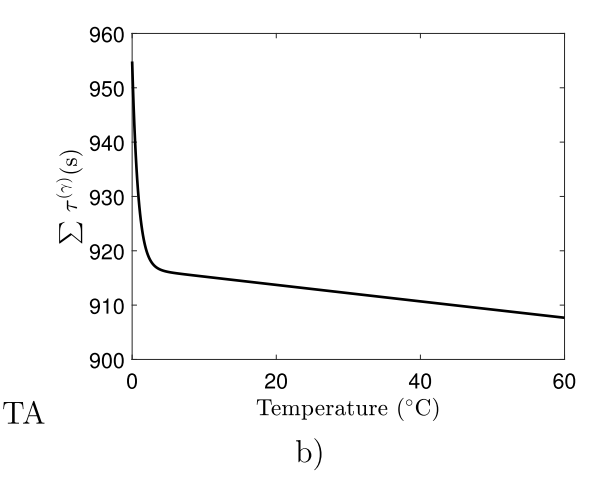
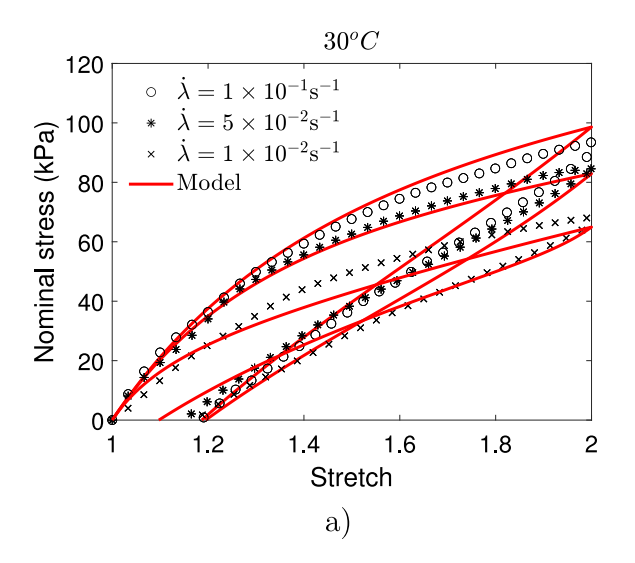


Fig. 12. (a) Overall time-dependent shear modulus function of temperature, and (b) overall relaxation time function of temperature.



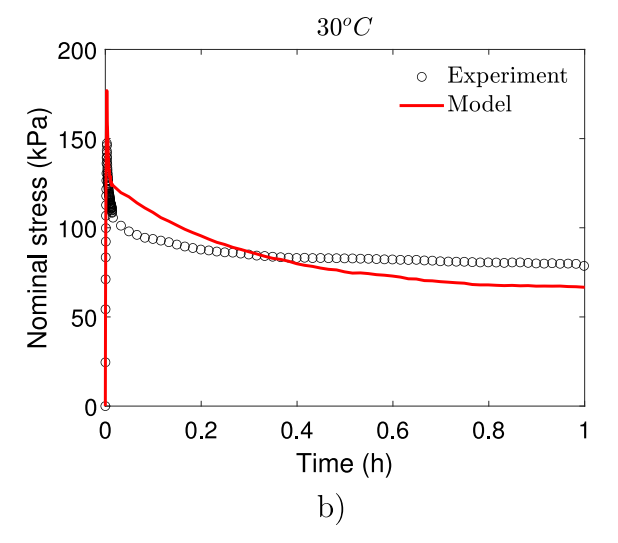


Fig. 13. Uniaxial model verification at 30 °C, a temperature not used for calibration, (a) load-unload, and (b) stress relaxation.

The evolution equation of each tensorial state dependent variable $\mathbf{A}^{(\gamma)}$ is given in the form

$$\dot{\mathbf{A}}^{(\gamma)} = \frac{1}{\hat{\mathbf{r}}^{(\gamma)}(\vartheta)} \left(\left(\mathbf{C}_{\mathrm{dis}} \right)^{-1} - \mathbf{A}^{(\gamma)} \right), \quad \mathbf{A}^{(\gamma)} \left(\mathbf{x}_{\mathrm{R}}, t = 0 \right) = \mathbf{1}, \tag{47}$$

where $\hat{\tau}^{(\gamma)}(\vartheta)$ is the temperature-dependent relaxation time for each viscous mechanism γ , and based on the data are taken as

$$\tau^{\gamma}(\vartheta) = \tau^{f(\gamma)} + \tau^{g(\gamma)} \exp\left(-\tau^{h(\gamma)}\vartheta\right). \tag{48}$$

5.1.1. Cauchy stress

Based on (30) and (41), straightforward calculations provide the Cauchy stress T in the form

$$\mathbf{T} = J^{-1}\mathbf{F} \left(2\frac{\partial \hat{\psi}_{\mathbf{R}}}{\partial \mathbf{C}} \right) \mathbf{F}^{\mathsf{T}}$$

$$= \underbrace{J^{-1} \left[\hat{G}_{\mathsf{TI}} \left(\boldsymbol{\vartheta} \right) \left(\mathbf{B}_{\mathsf{dis}} \right)_{0} + \hat{K}(\boldsymbol{\vartheta}) \left(\ln J \right) \mathbf{1} - 3\hat{K}(\boldsymbol{\vartheta}) \alpha (\boldsymbol{\vartheta} - \boldsymbol{\vartheta}_{0}) \mathbf{1} \right]}_{\mathsf{Time-independent \ contribution}}$$

$$+ J^{-1} \sum_{\gamma} \hat{G}_{\mathsf{TD}}^{(\gamma)} \left(\boldsymbol{\vartheta} \right) \left[\mathbf{F}_{\mathsf{dis}} \mathbf{A}^{(\gamma)} \mathbf{F}_{\mathsf{dis}}^{\mathsf{T}} - \frac{1}{3} \left(\mathbf{A}^{(\gamma)} : \mathbf{C}_{\mathsf{dis}} \right) \mathbf{1} \right], \tag{49}$$

$$\mathsf{Time-dependent \ contribution}$$

where the effective time-independent shear modulus $\hat{G}_{\text{TI}}(\vartheta) = \hat{G}_0(\vartheta) \left(\frac{\lambda_L}{3\bar{\lambda}}\right) \mathcal{L}^{-1}\left(\frac{\bar{\lambda}}{\lambda_L}\right)$ is a function of stretch and temperature.

5.1.2. Specialized constitutive equations for uniaxial tension

In the special case of uniaxial tension, and at a fixed reference known temperature and incompressible conditions, the constitutive model is simplified to a one-dimensional set of equations. In this case the Cauchy stress takes the form

$$\sigma = \hat{G}_{\text{TI}} \left(\vartheta_0 \right) \left[(\lambda)^2 - \frac{1}{\lambda} \right] + \sum_{\gamma} \hat{G}_{\text{TD}}^{(\gamma)} \left(\vartheta_0 \right) \left[(\lambda)^2 A^{(\gamma)} - \frac{1}{\lambda \sqrt{A^{(\gamma)}}} \right], \tag{50}$$

where σ is the Cauchy stress component in the loading direction. The evolution equation of each $A^{(\gamma)}$ in case of uniaxial tension is given in the form

$$\dot{A}^{(\gamma)} = \frac{1}{\hat{\tau}^{(\gamma)}(\theta_0)} \left((\lambda)^{-2} - A^{(\gamma)} \right). \tag{51}$$

In addition to that, the nominal stress is given by

$$P = \hat{G}_{\text{TI}}\left(\vartheta_0\right) \left[\lambda - \frac{1}{(\lambda)^2}\right] + \sum_{\gamma} \hat{G}_{\text{TD}}^{(\gamma)}\left(\vartheta_0\right) \left[\lambda A^{(\gamma)} - \frac{1}{(\lambda)^2 \sqrt{A^{(\gamma)}}}\right]$$
(52)

and can be used to directly compare the model with our experimental results.

6. Calibration

We calibrate the model in a uniaxial setting using (51) and (52) against the experimental results using the built-in MATLAB least

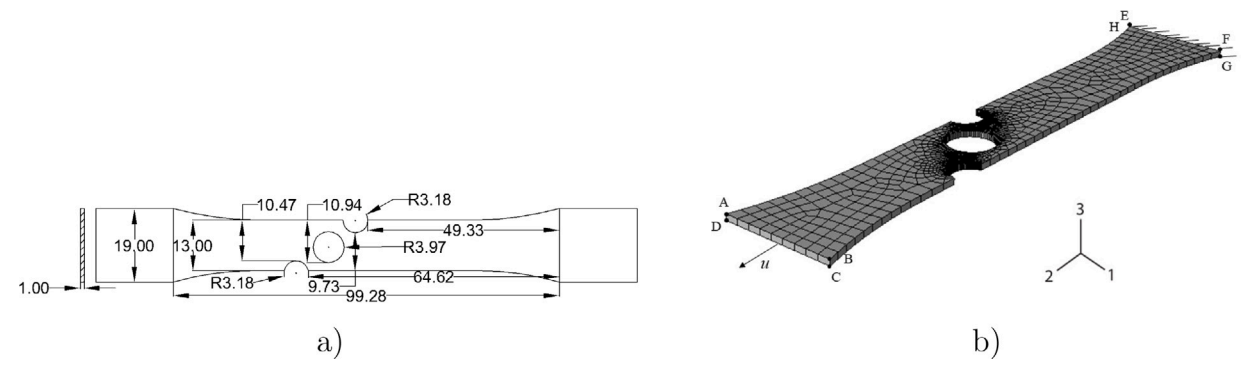


Fig. 14. VHB 4910 specimen used for the validation experiments. (a) Detailed geometry with dimensions in mm. (b) Undeformed finite element mesh with boundary conditions.

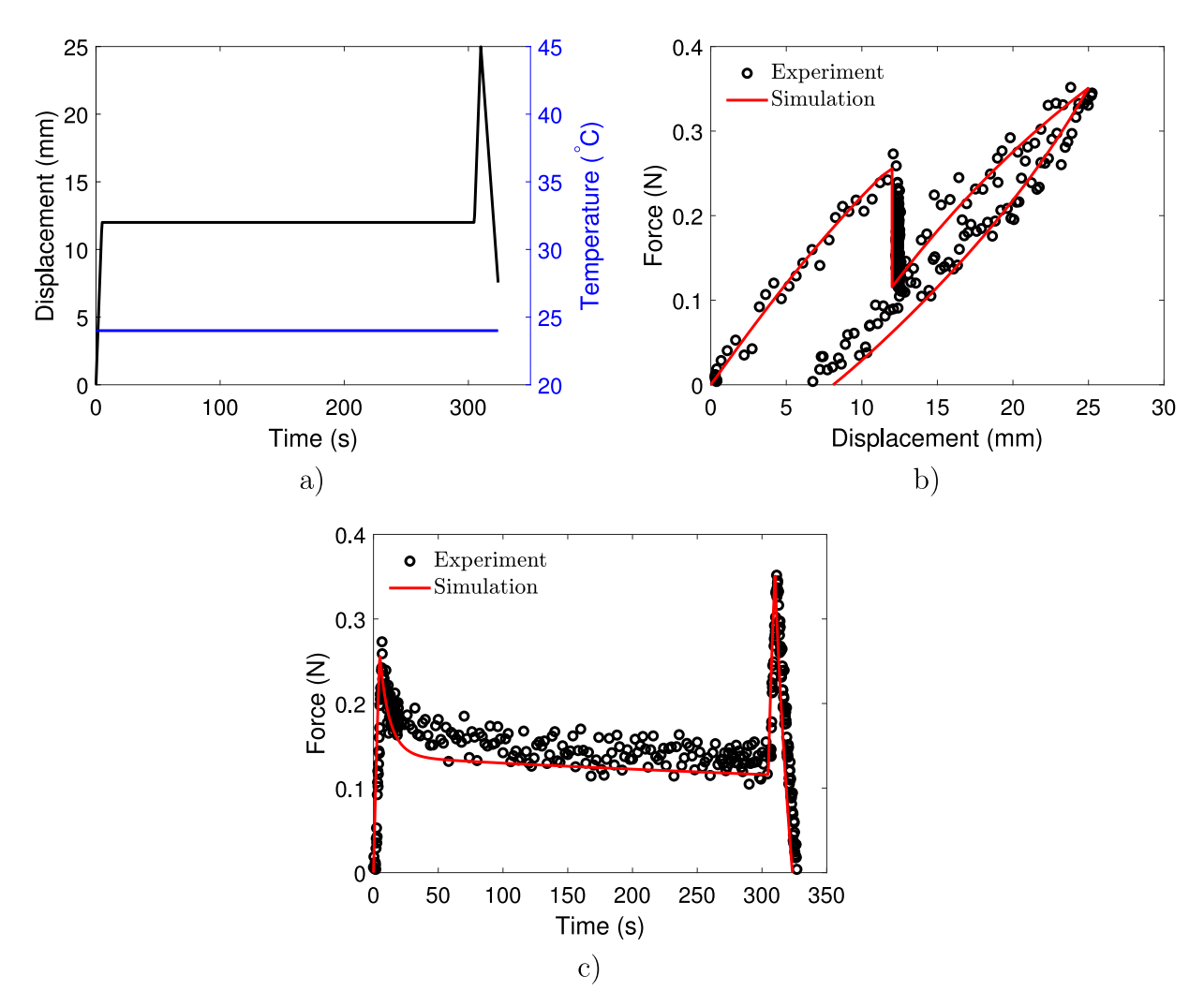


Fig. 15. Isothermal inhomogeneous model validation at 24 °C. (a) Prescribed displacement and temperature profiles, and the resulting (b) force-displacement curves, and (c) force-time curves.

squares function lsqnonlin. The calibration process involves multiple consecutive steps that build upon each other. First, we calibrate the time-independent parameters against the creep results reported in Fig. 5. The calibrated model shows a good agreement with the experimental data for all temperatures as can be seen in Fig. 9, and the material parameters G_m , G_b and λ_L are tabulated in Table 5.

Then, holding the time-independent parameters fixed, we calibrate the time-dependent parameters against the load–unload and relaxation results reported in Figs. 6 and 8, respectively. In order to capture the material behavior, we use three viscous mechanisms ($\gamma=3$) for the

 Table 5

 Calibrated time-independent material parameters.

G _m (Pa/K)	G_b (kPa)	λ_L
35.29	17.23	7.02

time-dependent contribution since we found that further increasing the number of viscous mechanisms did not lead to noticeably better results. The calibrated model along with the experimental data is shown in

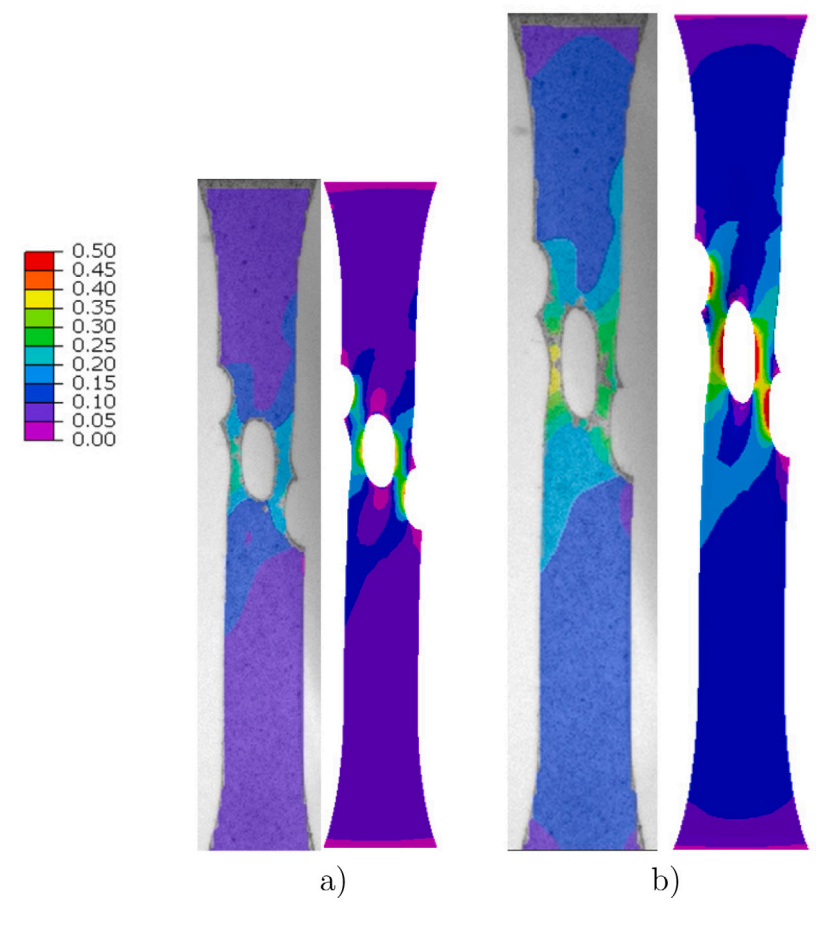


Fig. 16. Comparison of Hencky strain component E_{22} for the isothermal (24 °C) inhomogeneous uniaxial deformation between the experimentally measured (left) and simulated (right) validation at prescribed displacements of (a) 12 mm, and (b) 19.4 mm.

Table 6Calibrated time-dependent material parameters.

	$G^{c}_{ ext{TD}}^{(\gamma)}$ (kPa)	$G_{ ext{TD}}^{d}{}^{(\gamma)}$ (kPa)	$G^{e}_{ ext{TD}}^{(\gamma)}$ (kPa)	$ au^{f^{(\gamma)}}$ (s)	$ au^{g(\gamma)}$ (s)	$\tau^{h^{(\gamma)}}$ (s)	
$\gamma = 1$	12.29	97.93	6.31e-05	9.27	37.06	1.20	
$\gamma = 2$	17.45	157.96	0.05	4.23	1.00	1.03	
$\gamma = 3$	5.02	47.38	4.27e-05	484.21	419.06	3.66e-4	

Table 7 VHB 4910 thermal parameters.

Parameter	Value	Reference
κ	0.16 (W/m K)	3M (2020)
C	2010 (J/kg K)	Shan et al. (2013)
ρ	960 (kg/m^3)	3M (2020)

Figs. 10 and 11, and the calibrated time-dependent parameters are tabulated in Table 6. Lastly, to supplement the mechanical parameters, various thermal parameters from the VHB 4910 data sheet and the literature are tabulated in Table 7.

7. Model summary and behavior

It can be observed from the calibration of the time-independent behavior that VHB 4910 stiffens as temperature increases, which is an expected behavior for rubber-like materials. That can be observed by comparing the initial shear modulus $G_0(\vartheta)$ in (44) at different temperatures, where we observe a linear increase with a positive slope of $G_m=35.29\,\mathrm{Pa/K}$. Moreover, although the locking stretch λ_L is taken to be constant regardless of the temperature, the data indicates that as the temperature increases, the samples fail at a uniaxial stretch much lower

than room temperature intact samples. That alone is an interesting result, but we refrain from further exploration since it is outside the scope of this work. As for the time-dependent parameters, one can observe that an increase in temperature reduces the overall viscous contribution. Specifically, based on (46) as the temperature increases, all $G_{TD}^{(r)}$ show a decreasing trend as can be seen in Fig. 12a. Moreover, based on (48), the relaxation time $\tau^{(r)}$ for all viscous mechanisms also decreases with an increase in temperature as can be seen in Fig. 12b. On top of that, the sudden change in the sum of all relaxation times $\sum \tau^{(r)}$ for all viscous mechanisms occurs at \sim 4 °C, which may be attributed to the peak in the $\tan \delta$, as found in the DMA experiment discussed in Section 2.2.

These observations were expected based on our experimental results — the higher the temperature, the less viscous the material. Therefore, our constitutive model, by construction, is able to capture the effect of temperature on the rate-dependence, hysteresis and stress relaxation of VHB 4910.

To verify our constitutive model, we use the parameters provided in Tables 5 and 6 to predict the uniaxial behavior of VHB 4910 at 30 $^{\circ}\text{C}$, a temperature not used for parameter calibration. It can be observed from Fig. 13 that our model is in good agreement with the uniaxial experimental results at 30 $^{\circ}\text{C}$.

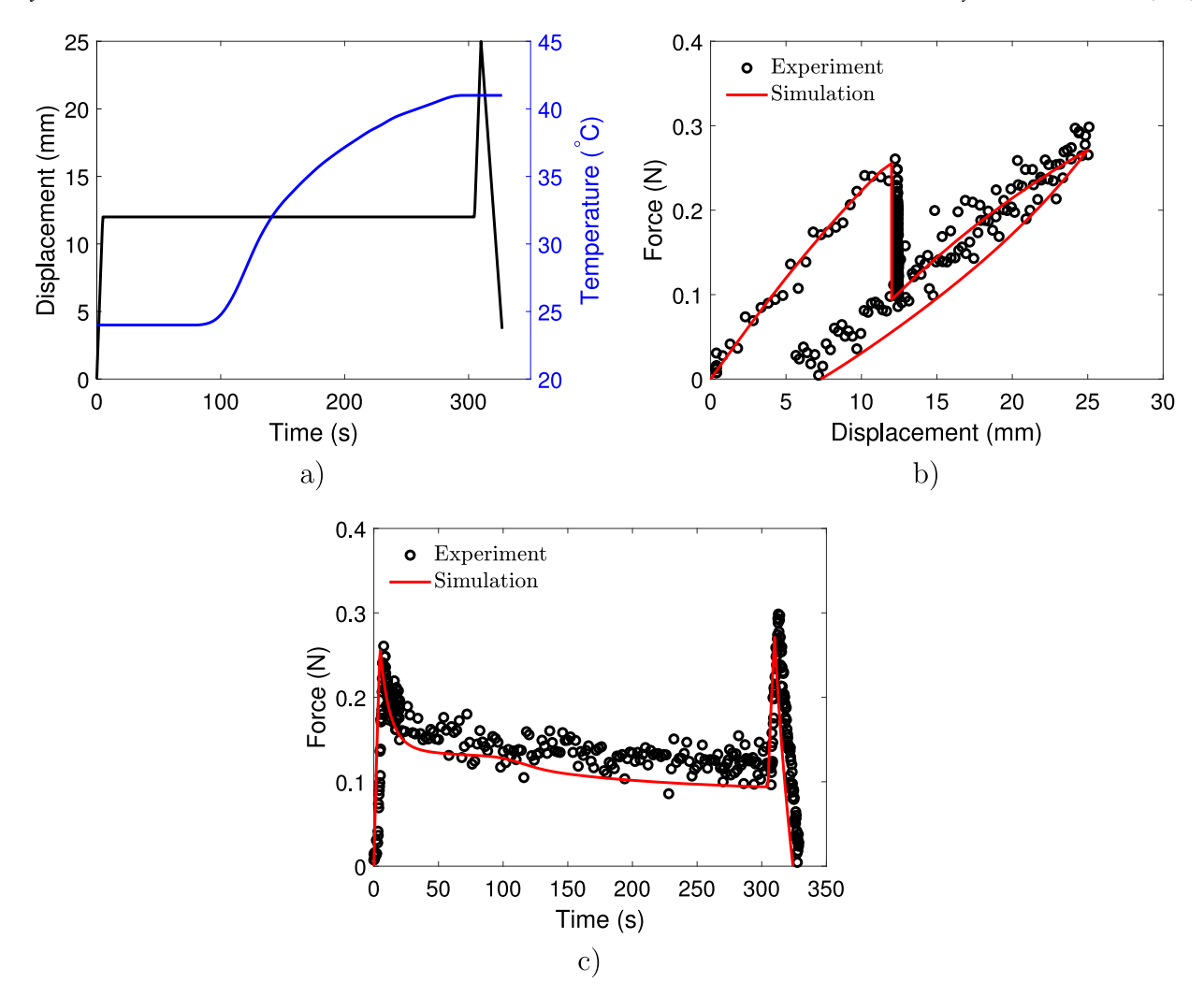


Fig. 17. Non-isothermal inhomogeneous model validation. (a) Prescribed displacement and temperature profiles, and the resulting (b) force-displacement curves, and (c) force-time curves.

8. Validation

In order to validate our constitutive model, we perform two inhomogeneous tension experiments, (i) isothermal at room temperature (24 $^{\circ}$ C), and (ii) non-isothermal. We then compare the reaction force and strain fields between the experimental and simulation results in order to validate our model.

The specimens used for validation are prepared by extracting dog bone samples using an ASTM D638-I cutting die. Then, three circular holes were punched out from the gauge section to create a tortuous geometry that will lead to an inhomogeneous deformation as shown in Fig. 14. Additionally, we spray paint the sample with a random speckle prior to the experiment, so that the full strain field can be measured using the DIC. Once more, we perform tension test using the same uniaxial testing machine, and we measure the strain field using the DIC, and the force using the 2.5 pound load cell.

As for the simulations, we implemented the constitutive model in Abaqus/Standard (2021) by writing a user material subroutine UMAT. The mesh of the geometry shown in Fig. 14b was discretized with 1427 C3D8T elements, with a single element through the thickness. Also, the boundary conditions can be observed from Fig. 14b; face EFGH is pinned ($\mathbf{u}=\mathbf{0}$) and the displacement measured from the experiment is prescribed on face ABCD in the 2 direction and constrained in the other directions. The total reaction force is obtained by summing up the reaction force from each node in the 2 direction on face EFGH. All remaining faces are traction free.

8.1. Isothermal at room temperature

The results for the isothermal room temperature validation are shown in Fig. 15. The displacement as a function of time is shown in Fig. 15a, and the comparison of both force–displacement and force–time curves is shown in Fig. 15b and c, respectively. From these results, one may clearly observe a good agreement between the experiment and the simulation. Furthermore, Fig. 16 also shows a good agreement between the experimental measured and simulated Hencky strain field component E_{22} at various times, where the Hencky strain is given by $\mathbf{E} = \ln \mathbf{U}$.

8.2. Non-isothermal

Similarly, the results for the non-isothermal validation are shown in Fig. 17. The displacement and temperature as a function of time are shown in Fig. 17a, and the comparison of both force–displacement and force–time curves is shown in Fig. 17b and c, respectively. From these results, one may clearly observe a good agreement between the experiment and the simulation. Furthermore, Fig. 18 also shows a good agreement between the experimental measured and simulated Hencky strain field component E_{22} at various times.

9. Conclusion

In this paper, we have developed an experimentally validated thermodynamically consistent, frame-indifferent, thermo-mechanically

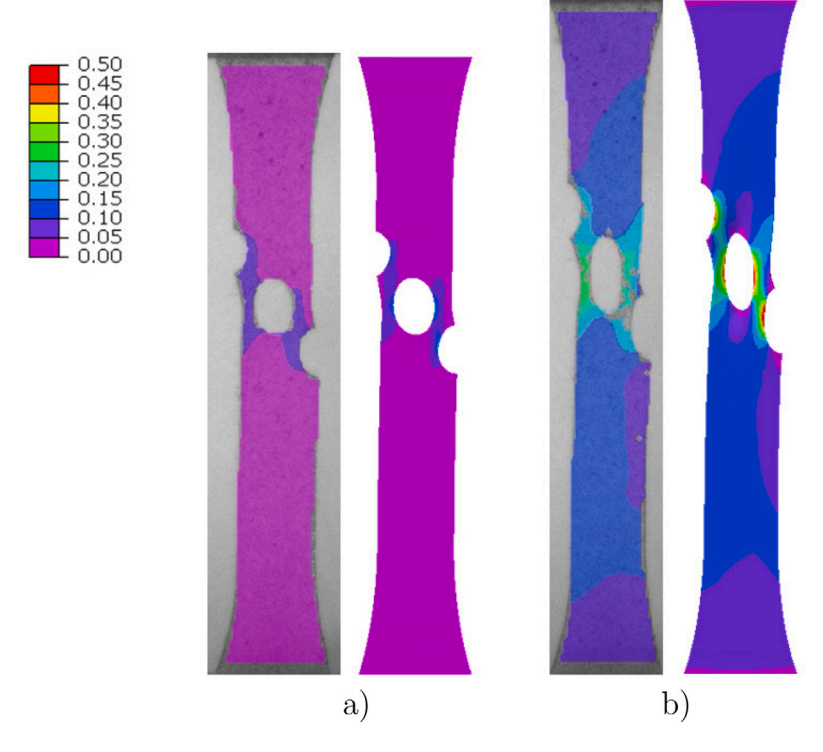


Fig. 18. Comparison of Hencky strain component E_{22} for the non-isothermal inhomogeneous uniaxial deformation between the experimentally measured (left) and simulated (right) validation at prescribed displacements of (a) 3.7 mm, and (b) 12.4 mm.

coupled constitutive theory for viscoelastomers. A suite of large deformation experiments were conducted at multiple stretch rates and temperatures on the industrially relevant material VHB. Based on the experiments, it was observed that the viscoelastic contribution to the overall behavior of VHB decreases when the temperature increases. The constitutive model is built upon the additive decomposition of the free energy into a time-independent contribution based on the Arruda-Boyce model (Arruda and Boyce, 1993), and a timedependent contribution based on the micromechanically motivated model of Linder et al. (2011). The model was then calibrated against the experimental data using non-linear least squares, and next implemented as a user element subroutine in the commercial finite elements software Abagus/Standard (2021). Finally, the model was validated by performing inhomogeneous deformation experiments and simulations under isothermal and non-isothermal conditions, and comparing various quantities such as the Hencky strain field, and the reaction force.

The novelty of this work is accounting for temperature effects on both the time-independent and time-dependent contributions, as well as validating the constitutive model in an inhomogeneous thermomechanically coupled setting. The validation in particular gives confidence that the continuum level constitutive model may be used for predictive simulation.

Despite being out of the scope of this study, we also observed that as the temperature increases, the samples fail at a uniaxial stretch lower than room temperatures samples. That is an important observation, especially when using VHB in applications involving elevated temperatures.

Acknowledgments

SAC acknowledges partial support from the National Science Foundation, USA under grant numbers (CMMI-1463121) and (CMMI-1751520). SN acknowledges partial support from the National Science Foundation, USA under grant numbers (CMMI-1652409) and (CMMI-2026717). HL acknowledges partial support from the Rutgers University Busch Biomedical Grant, USA.

Appendix A. Uniform temperature distribution across the sample

For systems where the heat transfer within an object is much faster than the heat transfer across the boundary, the full heat Eq. (40) may be simplified, leading to the so called lumped system analysis (Bergman et al., 2011). That assumption holds when the Biot number is

$$Bi = \frac{hL_c}{\kappa} \le 0.1. \tag{53}$$

where h is the convection coefficient, L_c the characteristic length, and κ the thermal conductivity.

Accordingly, we start by first calculating L_c for our samples having the length, width, and thickness at the gauge section of 9.49 mm, 3.18 mm, and 1 mm respectively, and we take the characteristic length to be given by the ratio of sample volume to surface area. Next, we estimate the convection coefficient based on the relationship for flow over a plate h=5.7+3.8V (McAdams, 1942) where V is the environment air velocity. Using an anemometer (BTMETER BT-866A) the air velocity inside the environment chamber was measured at 1.6 m/s. With κ from Table 7 one obtains Bi=0.028, and therefore lumped analysis is appropriate. Using a lumped analysis, the time for heating may be calculated using

$$t = \frac{\rho L_c C}{h} \ln \left(\frac{\theta_i - \theta_{\infty}}{\theta_c - \theta_{\infty}} \right), \tag{54}$$

where θ_i , θ_c , and θ_∞ are the initial room temperature, centerline temperature, and chamber temperature, respectively. Assuming the centerline temperature to be 99% of the chamber temperature θ_∞ , the time for the gauge section to reach a uniform temperature is $\approx 255\,\mathrm{s}$, or about 4 min. To verify our estimate, Fig. 19 shows the results of three monotonic tensile tests at a stretch rate of $10^{-1}\,\mathrm{s}^{-1}$ after holding the sample in the environmental chamber for 5 min, 10 min, and 15 min, respectively. We can clearly see that the results are almost identical, meaning that the sample temperature reaches a uniform distribution after 5 min only, which was expected. While both experiments and calculations show that 5 min is enough time to ensure a temperature uniformity across the sample, we choose to hold our samples for 15 min at temperature prior to the start of an experiment.

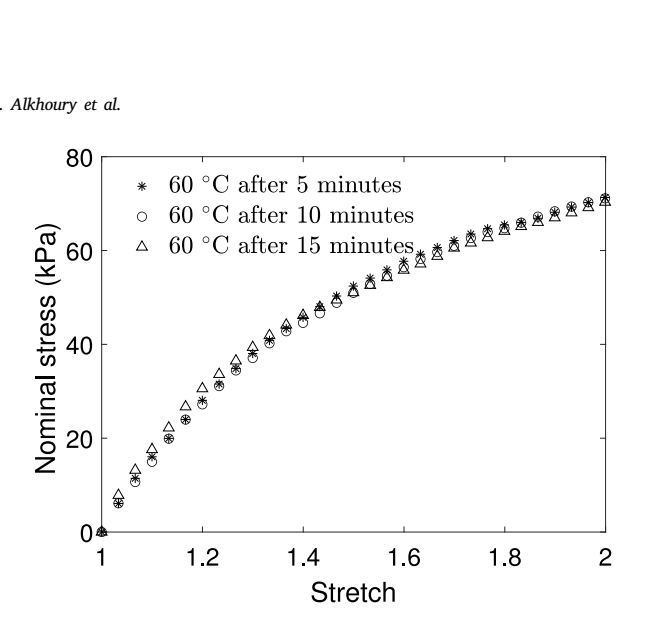


Fig. 19. Stress-stretch curves after holding the sample for 5 min, 10 min, and 15 min, respectively, at a temperature of 60 °C.

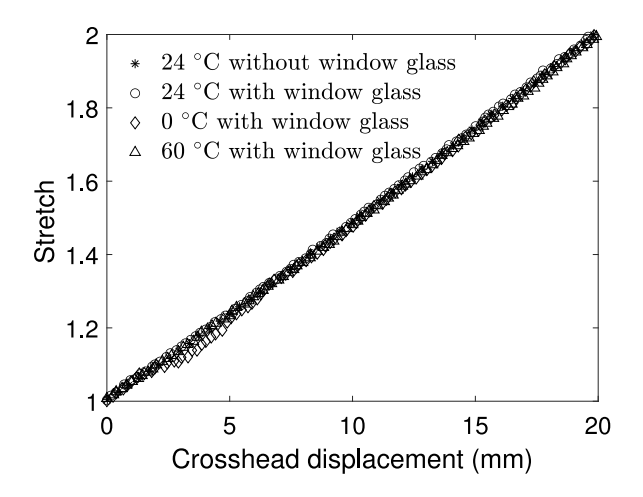


Fig. 20. Comparison of the DIC measured stretch as a function of the crosshead displacement with and without the environmental chamber window, and at different temperatures.

Appendix B. Verification of the DIC procedure

In this appendix we verify that the DIC procedures used in our experiments are unaffected by the environmental chamber window glass, and chamber temperature. In all cases that follow, we prescribe a constant crosshead velocity of $\dot{u} = 2.057$ mm/s.

First, to determine the affect of the environmental chamber window glass, samples were tested at room temperature with the door removed, and then samples were tested at room temperature with the door in place, both using the same setup described in Section 2.5 and the same prescribed loading conditions. Second, to determine the affect of the chamber temperature and window glass combined, samples were similarly tested with the environmental chamber window in place. For this scenario, we compare the prior experiments at room temperature with the environmental chamber door in place, to experiments maintaining both a cold temperature of 0 °C and elevated temperature of 60 °C with the environmental chamber door in place. Fig. 20, clearly indicates that for the range of temperatures under investigation in this work, the combined effect of the environmental chamber window glass and temperatures ranging from 0 °C up to 60 °C, there is no noticeable effect on the DIC measurement, and therefore we use DIC to measure the deformation in our experiments.

References

3M, 2020. 3M datasheet.

Abaqus/Standard, 2021. Abaqus Reference Manuals. Dassault Systemes Simulia, Providence, RI.

Ames, N.M., Srivastava, V., Chester, S.A., Anand, L., 2009. A thermo-mechanically coupled theory for large deformations of amorphous polymers. Part II: Applications. Int. J. Plast. 25 (8), 1495-1539.

Anand, L., Ames, N.M., Srivastava, V., Chester, S.A., 2009. A thermo-mechanically coupled theory for large deformations of amorphous polymers. Part I: Formulation. Int. J. Plast. (ISSN: 0749-6419) 25 (8), 1474-1494. http://dx.doi.org/10. 1016/j.ijplas.2008.11.004, URL https://www.sciencedirect.com/science/article/pii/ S0749641908001708.

Arruda, E.M., Boyce, M.C., 1993, A three-dimensional constitutive model for the large stretch behavior of rubber elastic materials. J. Mech. Phys. Solids 41 (2), 389-412.

Bergman, T.L., Incropera, F.P., DeWitt, D.P., Lavine, A.S., 2011. Fundamentals of Heat and Mass Transfer. John Wiley & Sons.

Bergström, J., Boyce, M., 1998. Constitutive modeling of the large strain timedependent behavior of elastomers. J. Mech. Phys. Solids (ISSN: 0022-5096) 46 (5), 931 - 954. http://dx.doi.org/10.1016/S0022-5096(97)00075-6, URL http://www. sciencedirect.com/science/article/pii/S0022509697000756.

Bosnjak, N., Nadimpalli, S., Okumura, D., Chester, S.A., 2020. Experiments and modeling of the viscoelastic behavior of polymeric gels. J. Mech. Phys. Solids 137, 103829

Bower, A.F., 2009. Applied Mechanics of Solids. CRC press.

Brochu, P., Pei, Q., 2010. Advances in dielectric elastomers for actuators and artificial muscles. Macromol. Rapid Commun. 31 (1), 10-36. http://dx.doi.org/ 10.1002/marc.200900425, URL https://onlinelibrary.wiley.com/doi/abs/10.1002/ marc.200900425.

Castro, F., Westbrook, K.K., Long, K.N., Shandas, R., Qi, H.J., 2010. Effects of thermal rates on the thermomechanical behaviors of amorphous shape memory polymers. Mech. Time-Dep. Mater. 14 (3), 219-241.

Chang, K., Soong, T., Oh, S.-T., Lai, M., 1995. Seismic behavior of steel frame with added viscoelastic dampers. J. Struct. Eng. 121 (10), 1418-1426.

Djoković, V., Kostoski, D., Dramićanin, M., 2000. Viscoelastic behavior of semicrystalline polymers at elevated temperatures on the basis of a two-process model for stress relaxation. J. Polym. Sci. B 38 (24), 3239-3246.

Drozdov, A., Christiansen, J.d., 2008. Thermo-viscoelastic and viscoplastic behavior of high-density polyethylene, Int. J. Solids Struct, 45 (14-15), 4274-4288

Guo, J., Xiao, R., Park, H.S., Nguyen, T.D., 2015. The temperature-dependent viscoelastic behavior of dielectric elastomers. J. Appl. Mech. 82 (9).

Gurtin, M.E., Fried, E., Anand, L., 2010. The Mechanics and Thermodynamics of Continua. Cambridge University Press.

Hossain, M., Liao, Z., 2020. An additively manufactured silicone polymer: Thermoviscoelastic experimental study and computational modelling. Additive Manuf. 35,

Hossain, M., Vu, D.K., Steinmann, P., 2012. Experimental study and numerical modelling of VHB 4910 polymer, Comput. Mater. Sci. 59, 65-74.

Jones, E., Reu, P., 2018. Distortion of digital image correlation (DIC) displacements and strains from heat waves. Exp. Mech. 58 (7), 1133-1156.

Jordan, B., Gorji, M.B., Mohr, D., 2020. Neural network model describing the temperature- and rate-dependent stress-strain response of polypropylene. Int. J. Plast. (ISSN: 0749-6419) 135, 102811. http://dx.doi.org/10. 1016/j.ijplas.2020.102811, URL https://www.sciencedirect.com/science/article/ pii/S074964191930419X.

Lakes, R.S., 2009. Viscoelastic Materials. Cambridge University Press.

Liao, Z., Hossain, M., Yao, X., Mehnert, M., Steinmann, P., 2020a. On thermoviscoelastic experimental characterization and numerical modelling of VHB polymer. Int. J. Non-Linear Mech. 118, 103263.

Liao, Z., Hossain, M., Yao, X., Navaratne, R., Chagnon, G., 2020b. A comprehensive thermo-viscoelastic experimental investigation of Ecoflex polymer. Polym. Test. 106478

Linder, C., Tkachuk, M., Miehe, C., 2011. A micromechanically motivated diffusionbased transient network model and its incorporation into finite rubber viscoelasticity. J. Mech. Phys. Solids 59 (10), 2134-2156.

Lion, A., 1997a. On the large deformation behaviour of reinforced rubber at different temperatures. J. Mech. Phys. Solids 45 (11-12), 1805-1834.

Lion, A., 1997b. A physically based method to represent the thermo-mechanical behaviour of elastomers. Acta Mech. 123 (1), 1-25.

Liu, Y., Gall, K., Dunn, M.L., Greenberg, A.R., Diani, J., 2006. Thermomechanics of shape memory polymers: uniaxial experiments and constitutive modeling. Int. J. Plast. 22 (2), 279-313.

Ma, C., Zeng, Z., Zhang, H., Rui, X., 2019. A correction method for heat wave distortion in digital image correlation measurements based on background-oriented schlieren. Appl. Sci. 9 (18), 3851.

Mao, Y., Lin, S., Zhao, X., Anand, L., 2017. A large deformation viscoelastic model for double-network hydrogels, J. Mech. Phys. Solids (ISSN: 0022-5096) $100,\ 103-130.\ http://dx.doi.org/10.1016/j.jmps.2016.12.011,\ URL\ https://www.$ sciencedirect.com/science/article/pii/S0022509616308389.

McAdams, W.H., 1942. Heat Transmission. McGraw-hill.

- Mehnert, M., Hossain, M., Steinmann, P., 2018. Numerical modeling of thermo-electroviscoelasticity with field-dependent material parameters. Int. J. Non-Linear Mech. (ISSN: 0020-7462) 106, 13–24. http://dx.doi.org/10.1016/j.ijnonlinmec.2018.08. 016, URL https://www.sciencedirect.com/science/article/pii/S0020746218302981.
- Mehnert, M., Hossain, M., Steinmann, P., 2021a. A complete thermo–electro–viscoelastic characterization of dielectric elastomers, Part I: Experimental investigations. J. Mech. Phys. Solids (ISSN: 0022-5096) 157, 104603. http://dx.doi.org/10. 1016/j.jmps.2021.104603, URL https://www.sciencedirect.com/science/article/pii/ S0022509621002465.
- Mehnert, M., Hossain, M., Steinmann, P., 2021b. A complete thermo-electro-viscoelastic characterization of dielectric elastomers, Part II: Continuum modeling approach. J. Mech. Phys. Solids (ISSN: 0022-5096) 157, 104625. http://dx.doi.org/10. 1016/j.jmps.2021.104625, URL https://www.sciencedirect.com/science/article/pii/ S0022509621002660.
- Mirfakhrai, T., Madden, J.D., Baughman, R.H., 2007. Polymer artificial muscles. Mater. Today 10 (4), 30–38.
- Nguyen, T.D., Jerry Qi, H., Castro, F., Long, K.N., 2008. A thermoviscoelastic model for amorphous shape memory polymers: Incorporating structural and stress relaxation. J. Mech. Phys. Solids (ISSN: 0022-5096) 56 (9), 2792–2814. http://dx.doi.org/10. 1016/j.jmps.2008.04.007, URL https://www.sciencedirect.com/science/article/pii/ S0022509608000951.
- O'Halloran, A., O'malley, F., McHugh, P., 2008. A review on dielectric elastomer actuators, technology, applications, and challenges. J. Appl. Phys. 104 (7), 9.
- Plante, J.-S., Dubowsky, S., 2006. Large-scale failure modes of dielectric elastomer actuators. Int. J. Solids Struct. (ISSN: 0020-7683) 43 (25), 7727–7751. http://dx.doi.org/10.1016/j.ijsolstr.2006.03.026, URL https://www.sciencedirect.com/science/article/pii/S0020768306000990.
- Qi, H.J., Nguyen, T.D., Castro, F., Yakacki, C.M., Shandas, R., 2008. Finite deformation thermo-mechanical behavior of thermally induced shape memory polymers. J. Mech. Phys. Solids (ISSN: 0022-5096) 56 (5), 1730–1751. http://dx.doi.org/10. 1016/j.jmps.2007.12.002, URL https://www.sciencedirect.com/science/article/pii/ S002250960700230X.
- Rasband, W., 1997-2018. ImageJ. U. S. National Institutes of Health, Bethesda, MD.
 Reese, S., 2003. A micromechanically motivated material model for the thermoviscoelastic material behaviour of rubber-like polymers. Int. J. Plast. 19 (7), 909-940.

- Reese, S., Govindjee, S., 1997. Theoretical and numerical aspects in the thermoviscoelastic material behaviour of rubber-like polymers. Mech. Time-Dep. Mater. 1 (4), 357–396.
- Reese, S., Govindjee, S., 1998. A theory of finite viscoelasticity and numerical aspects. Int. J. Solids Struct. 35 (26-27), 3455–3482.
- Sain, T., Loeffel, K., Chester, S., 2018. A thermo-chemo-mechanically coupled constitutive model for curing of glassy polymers. J. Mech. Phys. Solids (ISSN: 0022-5096) 116, 267–289. http://dx.doi.org/10.1016/j.jmps.2018.04.001, URL https://www.sciencedirect.com/science/article/pii/S0022509617311328.
- Santapuri, S., Lowe, R.L., Bechtel, S.E., Dapino, M.J., 2013. Thermodynamic modeling of fully coupled finite-deformation thermo-electro-magneto-mechanical behavior for multifunctional applications. Int. J. Eng. Sci. (ISSN: 0020-7225) 72, 117–139. http://dx.doi.org/10.1016/j.ijengsci.2013.06.011, URL https://www.sciencedirect. com/science/article/pii/S002072251300102X.
- Shan, W., Lu, T., Majidi, C., 2013. Soft-matter composites with electrically tunable elastic rigidity. Smart Mater. Struct. 22 (8), 085005.
- Shen, K., Soong, T., 1995. Modeling of viscoelastic dampers for structural applications. J. Eng. Mech. 121 (6), 694–701.
- Srivastava, V., Chester, S.A., Ames, N.M., Anand, L., 2010a. A thermo-mechanically-coupled large-deformation theory for amorphous polymers in a temperature range which spans their glass transition. Int. J. Plast. 26 (8), 1138–1182.
- Srivastava, V., Chester, S.A., Anand, L., 2010b. Thermally actuated shape-memory polymers: Experiments, theory, and numerical simulations. J. Mech. Phys. Solids 58 (8), 1100–1124.
- Valanis, K., 1966. Thermodynamics of large viscoelastic deformations. J. Math. Phys. 45 (1-4), 197–212.
- Wang, S., Decker, M., Henann, D.L., Chester, S.A., 2016. Modeling of dielectric viscoelastomers with application to electromechanical instabilities. J. Mech. Phys. Solids 95, 213–229.
- Wissler, M., Mazza, E., 2007. Mechanical behavior of an acrylic elastomer used in dielectric elastomer actuators. Sensors Actuators A (ISSN: 0924-4247) 134 (2), 494– 504. http://dx.doi.org/10.1016/j.sna.2006.05.024, URL https://www.sciencedirect. com/science/article/pii/S0924424706003803.
- Yang, L., Yang, L., Lowe, R.L., 2021. A viscoelasticity model for polymers: time, temperature, and hydrostatic pressure dependent young's modulus and poisson's ratio across transition temperatures and pressures. Mech. Mater. (ISSN: 0167-6636) 157, 103839. http://dx.doi.org/10.1016/j.mechmat.2021.103839, URL https://www.sciencedirect.com/science/article/pii/S0167663621000922.